Imprint of SUSY in radiative *B*-meson decays

Helmut Eberl,[1] Keisho Hidaka,[2] Elena Ginina,[1,3] and Akimasa Ishikawa[4,5,6]

[1]*Institut für Hochenergiephysik der Österreichischen Akademie der Wissenschaften, A-1050 Vienna, Austria*

[2]*Department of Physics, Tokyo Gakugei University, Koganei, Tokyo 184-8501, Japan*

[3]*VRVis Zentrum für Virtual Reality und Visualisierung Forschungs-GmbH, A-1220 Vienna, Austria*

[4]*Institute of Particle and Nuclear Studies, High Energy Accelerator Research Organization (KEK), Ibaraki 305-0801, Japan*

[5]*The Graduate University for Advanced Studies (SOKENDAI), Hayama 240-0193, Japan*

[6]*International Center for Elementary Particle Physics, University of Tokyo, Tokyo 113-0033, Japan*

(Received 1 July 2021; accepted 16 September 2021; published 19 October 2021)

We study supersymmetric (SUSY) effects on $C_7(\mu_b)$ and $C_7'(\mu_b)$ which are the Wilson coefficients (WCs) for $b \to s\gamma$ at b-quark mass scale μ_b and are closely related to radiative B-meson decays. The SUSY-loop contributions to $C_7(\mu_b)$ and $C_7'(\mu_b)$ are calculated at leading order (LO) in the Minimal Supersymmetric Standard Model (MSSM) with general quark-flavor violation (QFV). For the first time we perform a systematic MSSM parameter scan for the WCs $C_7(\mu_b)$ and $C_7'(\mu_b)$ respecting all the relevant constraints, i.e., the theoretical constraints from vacuum stability conditions and the experimental constraints, such as those from K- and B-meson data and electroweak precision data, as well as recent limits on SUSY particle masses and the 125 GeV Higgs boson data from LHC experiments. From the parameter scan we find the following: (1) The MSSM contribution to $\mathrm{Re}(C_7(\mu_b))$ can be as large as $\sim \pm 0.05$, which could correspond to about 3σ significance of New Physics (NP) signal in the future LHCb and Belle II experiments. (2) The MSSM contribution to $\mathrm{Re}(C_7'(\mu_b))$ can be as large as ~ -0.08, which could correspond to about 4σ significance of NP signal in the future LHCb and Belle II experiments. (3) These large MSSM contributions to the WCs are mainly due to (i) large scharm-stop mixing and large scharm/stop involved trilinear couplings T_{U23}, T_{U32} and T_{U33}, (ii) large sstrange-sbottom mixing and large sstrange-sbottom involved trilinear couplings T_{D23}, T_{D32} and T_{D33} and (iii) large bottom Yukawa coupling Y_b for large $\tan\beta$ and large top Yukawa coupling Y_t. In case such large NP contributions to the WCs are really observed in the future experiments at Belle II and the LHCb Upgrade, this could be the imprint of QFV SUSY (the MSSM with general QFV) and would encourage to perform further studies of the WCs $C_7'(\mu_b)$ and $C_7^{\mathrm{MSSM}}(\mu_b)$ at higher order (NLO/NNLO) level in this model.

DOI: 10.1103/PhysRevD.104.075025

I. INTRODUCTION

Our present knowledge of elementary particle physics is very successfully described by the Standard Model (SM) of electroweak and strong interactions. This model has, however, several essential problems, such as naturalness and hierarchy problems. Moreover, it can not explain observed phenomena like the neutrino masses and mixings, the matter-antimatter asymmetry in our universe, and the origin of dark matter. Hence, it is necessary to search for New Physics (NP) theory that solves these problems. The theory of supersymmetry (SUSY) is still the most prominent candidate for such a NP theory solving the SM problems.

Here we study the influence of SUSY on $C_7(\mu_b)$ and $C_7'(\mu_b)$ which are the Wilson coefficients (WCs) for the quark flavor changing transition $b \to s\gamma$ at the b-quark mass scale μ_b. They are closely related to radiative B-meson decays. We calculate the SUSY-loop contributions to $C_7(\mu_b)$ and $C_7'(\mu_b)$ at leading order (LO) in the Minimal Supersymmetric Standard Model (MSSM) with general quark-flavor violation (QFV) due to squark generation mixing. In the numerical computation of the WCs, we perform a MSSM parameter scan respecting all the relevant theoretical and experimental constraints, such as those from vacuum stability conditions, those from K- and B-meson data, the 125 GeV Higgs boson data from LHC, and electroweak precision data, as well as recent limits on SUSY particle (sparticle) masses from LHC experiments.

On the experimental side, the WCs $C_7(\mu_b)$ and $C_7'(\mu_b)$ can be measured precisely in the ongoing and future experiments at Belle II and LHCb Upgrade [1–4]. There are many papers studying the radiative B-meson decays in the SM [5–12], the 2HDMs (Two-Higgs Doublet models) [13–15] and the MSSM [16–20].

However, there is no systematic numerical study on the SUSY-loop contributions to $C_7(\mu_b)$ and $C_7'(\mu_b)$ *even at LO* in the MSSM with general QFV.[1] In this paper we thoroughly perform such a systematic study with special emphasis on the importance of SUSY QFV in order to clarify a possibility that an imprint of SUSY can be found in radiative B-meson decays, focusing on the WCs $C_7(\mu_b)$ and $C_7'(\mu_b)$.

In the phenomenological study of the MSSM, usually quark-flavor conservation (QFC) is assumed, except for the quark-flavor violation stemming from the Cabibbo-Kobayashi-Maskawa (CKM) matrix. However, in general there can be SUSY QFV terms in the squark mass matrix. Especially important QFV terms are the mixing terms between the 2nd and the 3rd squark generations, such as $\tilde{c}_{L,R}$-$\tilde{t}_{L,R}$ and $\tilde{s}_{L,R}$-$\tilde{b}_{L,R}$ mixing terms, where $\tilde{c}$, $\tilde{t}$, $\tilde{s}$ and $\tilde{b}$ are the charm-, top-, strange- and bottom-squark, respectively. In this study we put special emphasis on the influence of the SUSY QFV due to $\tilde{c}_{L,R}$-$\tilde{t}_{L,R}$ and $\tilde{s}_{L,R}$-$\tilde{b}_{L,R}$ mixings on the WCs $C_7(\mu_b)$ and $C_7'(\mu_b)$.

In our analysis we assume that there is no SUSY lepton-flavor violation. We also assume that R-parity is conserved and that the lightest neutralino $\tilde{\chi}_1^0$ is the lightest SUSY particle (LSP). We work in the MSSM with real parameters, except for the CKM matrix.

In the following section we introduce the SUSY QFV parameters originating from the squark mass matrices. Details about our parameters scan are given in Sec. III. In Sec. IV we define the relevant WCs and analyze their behavior in the MSSM with QFV. The conclusions are in Sec. V. All relevant constraints are listed in Appendix A.

II. SQUARK MASS MATRICES IN THE MSSM WITH FLAVOR VIOLATION

In the super-CKM basis of $\tilde{q}_{0\gamma}=(\tilde{q}_{1\mathrm{L}},\tilde{q}_{2\mathrm{L}},\tilde{q}_{3\mathrm{L}},\tilde{q}_{1\mathrm{R}},\tilde{q}_{2\mathrm{R}},\tilde{q}_{3\mathrm{R}})$, $\gamma=1,\ldots6$, with $(q_1,q_2,q_3)=(u,c,t)$, (d,s,b), the up-type and down-type squark mass matrices $\mathcal{M}^2_{\tilde{q}}, \tilde{q}=\tilde{u},\tilde{d}$, at the SUSY scale have the following most general 3×3 block form [22]:

$$\mathcal{M}^2_{\tilde{q}}=\begin{pmatrix}\mathcal{M}^2_{\tilde{q},LL} & \mathcal{M}^2_{\tilde{q},LR}\\ \mathcal{M}^2_{\tilde{q},RL} & \mathcal{M}^2_{\tilde{q},RR}\end{pmatrix}, \qquad \tilde{q}=\tilde{u},\tilde{d}. \tag{1}$$

Non-zero off-diagonal terms of the 3×3 blocks $\mathcal{M}^2_{\tilde{q},LL}$, $\mathcal{M}^2_{\tilde{q},RR}$, $\mathcal{M}^2_{\tilde{q},LR}$ and $\mathcal{M}^2_{\tilde{q},RL}$ in Eq. (1) explicitly break quark-flavor in the squark sector of the MSSM. The left-left and right-right blocks in Eq. (1) are given by

$$\begin{aligned}\mathcal{M}^2_{\tilde{u}(\tilde{d}),LL}&=M^2_{Q_{u(d)}}+D_{\tilde{u}(\tilde{d}),LL}\mathbf{1}+\hat{m}^2_{u(d)},\\ \mathcal{M}^2_{\tilde{u}(\tilde{d}),RR}&=M^2_{U(D)}+D_{\tilde{u}(\tilde{d}),RR}\mathbf{1}+\hat{m}^2_{u(d)},\end{aligned} \tag{2}$$

where $M^2_{Q_u}=V_{\mathrm{CKM}}M^2_{Q}V^\dagger_{\mathrm{CKM}}$, $M^2_{Q_d}\equiv M^2_Q$, $M_{Q,U,D}$ are the Hermitian soft SUSY-breaking mass matrices of the squarks, $D_{\tilde{u}(\tilde{d}),LL}$, $D_{\tilde{u}(\tilde{d}),RR}$ are the D-terms, and $\hat{m}_{u(d)}$ are the diagonal mass matrices of the up(down)-type quarks. $M^2_{Q_u}$ is related with $M^2_{Q_d}$ by the CKM matrix V_{CKM} due to the $SU(2)_{\mathrm{L}}$ symmetry. The left-right and right-left blocks of Eq. (1) are given by

$$\begin{aligned}\mathcal{M}^2_{\tilde{u}(\tilde{d}),RL}&=\mathcal{M}^{2\dagger}_{\tilde{u}(\tilde{d}),LR}\\ &=\frac{v_2(v_1)}{\sqrt{2}}T_{U(D)}-\mu^*\hat{m}_{u(d)}\cot\beta(\tan\beta),\end{aligned} \tag{3}$$

where $T_{U,D}$ are the soft SUSY-breaking trilinear coupling matrices of the up-type and down-type squarks entering the Lagrangian $\mathcal{L}_{\mathrm{int}}\supset-(T_{U\alpha\beta}\tilde{u}^\dagger_{R\alpha}\tilde{u}_{L\beta}H^0_2+T_{D\alpha\beta}\tilde{d}^\dagger_{R\alpha}\tilde{d}_{L\beta}H^0_1)$, μ is the higgsino mass parameter, and $\tan\beta=v_2/v_1$ with $v_{1,2}=\sqrt{2}\langle H^0_{1,2}\rangle$. The squark mass matrices are diagonalized by the 6×6 unitary matrices $U^{\tilde{q}}$, $\tilde{q}=\tilde{u},\tilde{d}$, such that

$$U^{\tilde{q}}\mathcal{M}^2_{\tilde{q}}(U^{\tilde{q}})^\dagger=\mathrm{diag}(m^2_{\tilde{q}_1},\ldots,m^2_{\tilde{q}_6}), \tag{4}$$

with $m_{\tilde{q}_1}<\ldots<m_{\tilde{q}_6}$. The physical mass eigenstates $\tilde{q}_i, i=1,\ldots,6$ are given by $\tilde{q}_i=U^{\tilde{q}}_{i\alpha}\tilde{q}_{0\alpha}$.

In this paper we focus on the $\tilde{c}_L-\tilde{t}_L$, $\tilde{c}_R-\tilde{t}_R$, $\tilde{c}_R-\tilde{t}_L$, $\tilde{c}_L-\tilde{t}_R$, $\tilde{s}_L-\tilde{b}_L$, $\tilde{s}_R-\tilde{b}_R$, $\tilde{s}_R-\tilde{b}_L$, and $\tilde{s}_L-\tilde{b}_R$ mixing which is described by the QFV parameters $M^2_{Q_u23}\simeq M^2_{Q23}$, M^2_{U23}, T_{U23}, T_{U32}, M^2_{Q23}, M^2_{D23}, T_{D23} and T_{D32}, respectively. We will also often refer to the QFC parameter T_{U33} and T_{D33} which induces the $\tilde{t}_L-\tilde{t}_R$ and $\tilde{b}_L-\tilde{b}_R$ mixing, respectively, and plays an important role in this study.

The slepton parameters are defined analogously to the squark ones. All the parameters in this study are assumed to be real, except the CKM matrix V_{CKM}.

III. PARAMETER SCAN

In our MSSM-parameter scan we take into account theoretical constraints from vacuum stability conditions and experimental constraints from K- and B-meson data, the H^0 mass and coupling data and electroweak precision

[1]To our knowledge, there is no complete next to leading order (NLO) computation of WCs $C_7(\mu_b)$ and $C_7'(\mu_b)$ in the MSSM with general QFV in the present literature. In [21] gluino-squark loop contributions to the WCs $C_{7,8}(\mu_W)$ and $C'_{7,8}(\mu_W)$ at the weak scale μ_W are calculated at NLO of SUSY-QCD in the MSSM with general QFV. However, they did not perform a complete NLO computation of $C_7(\mu_b)$ and $C_7'(\mu_b)$. Here we remark that in [13,14] the charged Higgs boson loop contributions to the WCs $C_{7,8}(\mu_W)$ and $C_7(\mu_b)$ are calculated at NLO of QCD in the 2HDMs.

TABLE I. Scanned ranges and fixed values of the MSSM parameters (in units of GeV or GeV^2, except for $\tan\beta$). The parameters that are not shown explicitly are taken to be zero. $M_{1,2,3}$ are the U(1), SU(2), SU(3) gaugino mass parameters.

$\tan\beta$	M_1	M_2	M_3	μ	m_A(pole)
$10 \div 80$	$100 \div 2500$	$100 \div 2500$	$2500 \div 5000$	$100 \div 2500$	$1350 \div 6000$
M^2_{Q22}	M^2_{Q33}	$\lvert M^2_{Q23}\rvert$	M^2_{U22}	M^2_{U33}	$\lvert M^2_{U23}\rvert$
$2500^2 \div 4000^2$	$2500^2 \div 4000^2$	$<1000^2$	$1000^2 \div 4000^2$	$600^2 \div 3000^2$	$<2000^2$
M^2_{D22}	M^2_{D33}	$\lvert M^2_{D23}\rvert$	$\lvert T_{U23}\rvert$	$\lvert T_{U32}\rvert$	$\lvert T_{U33}\rvert$
$2500^2 \div 4000^2$	$1000^2 \div 3000^2$	$<2000^2$	<4000	<4000	<5000
$\lvert T_{D23}\rvert$	$\lvert T_{D32}\rvert$	$\lvert T_{D33}\rvert$	$\lvert T_{E33}\rvert$		
<3000	<3000	<4000	<500		

M^2_{Q11}	M^2_{U11}	M^2_{D11}	M^2_{L11}	M^2_{L22}	M^2_{L33}	M^2_{E11}	M^2_{E22}	M^2_{E33}
4500^2	4500^2	4500^2	1500^2	1500^2	1500^2	1500^2	1500^2	1500^2

data, as well as limits on SUSY particle masses from recent LHC experiments (see Appendix A). Here H^0 is the discovered SM-like Higgs boson which we identify as the lightest CP even neutral Higgs boson h^0 in the MSSM. Concerning squark generation mixings, we only consider the mixing between the second and third generation of squarks. The mixing between the first and the second generation squarks is strongly constrained by the K- and D-meson data [23,24]. The experimental constraints on the mixing of the first and third generation squarks are not so strong [25], but we do not consider this mixing since its effect is essentially similar to that of the mixing of the second and third generation squarks. We generate the input parameter points by using random numbers in the ranges shown in Table I, where some parameters are fixed as given in the last box. All input parameters are $\overline{\rm DR}$ parameters defined at scale Q = 1 TeV, except m_A(pole) which is the pole mass of the CP odd Higgs boson A^0. The parameters that are not shown explicitly are taken to be zero. The entire scan lies in the decoupling Higgs limit, i.e., in the scenarios with large $\tan\beta \geq 10$ and large $m_A \geq$ 1350 GeV (see Table I), respecting the fact that the discovered Higgs boson is SM-like. It is well known that the lightest MSSM Higgs boson h^0 is SM-like (including its couplings) in this limit. We do not assume a GUT relation for the gaugino masses M_1, M_2, M_3.

All MSSM input parameters are taken as $\overline{\rm DR}$ parameters at the scale $Q = 1$ TeV, except m_A(pole), and then are transformed by RGEs to those at the weak scale of $Q = \mu_W$ for the computation of the WCs $C_{7,8}(\mu_W)$ and $C'_{7,8}(\mu_W)$ in the MSSM. The masses and rotation matrices of the sfermions are renormalized at one-loop level by using the public code SPheno-v3.3.8 [26,27] based on the technique given in [28].

From 8660000 input points generated in the scan 72904 points survived all constraints. These are 0.84%. We show these survival points in all scatter plots in this article.

IV. WC $C_7(\mu_b)$ AND $C'_7(\mu_b)$ IN THE MSSM WITH QFV

The effective Hamiltonian for the radiative transition $b \to s\gamma$ is given by

$$H_{\rm eff} = -\frac{4G_F}{\sqrt{2}} V_{tb}V^*_{ts} \sum_i C_i O_i, \tag{5}$$

where G_F is the Fermi constant and $V_{tb}V^*_{ts}$ is a CKM factor. The operators relevant to $b \to s\gamma$ are

$$\begin{aligned} O_2 &= \bar{s}_L \gamma_\mu c_L \bar{c}_L \gamma^\mu b_L, \\ O_7 &= \frac{e}{16\pi^2} m_b \bar{s}_L \sigma^{\mu\nu} b_R F_{\mu\nu}, \\ O_8 &= \frac{g_s}{16\pi^2} m_b \bar{s}_L \sigma^{\mu\nu} T^a b_R G^a_{\mu\nu}, \end{aligned} \tag{6}$$

and their chirality counterparts

$$\begin{aligned} O'_2 &= \bar{s}_R \gamma_\mu c_R \bar{c}_R \gamma^\mu b_R, \\ O'_7 &= \frac{e}{16\pi^2} m_b \bar{s}_R \sigma^{\mu\nu} b_L F_{\mu\nu}, \\ O'_8 &= \frac{g_s}{16\pi^2} m_b \bar{s}_R \sigma^{\mu\nu} T^a b_L G^a_{\mu\nu}, \end{aligned} \tag{7}$$

where m_b is the bottom quark mass, e and g_s are the electromagnetic and strong coupling, $F_{\mu\nu}$ and $G^a_{\mu\nu}$ the $U(1)_{\rm em}$ and $SU(3)_c$ field-strength tensors, T^a are color generators, and the indices L,R denote the chirality of the quark fields. Here note that the SM contributions to $C'_{2,7,8}(\mu_W)$ are (almost) zero at LO. The WCs $C_7(\mu_b)$ and $C'_7(\mu_b)$ at the bottom quark mass scale μ_b can be measured precisely in the experiments at Belle II and LHCb Upgrade [1–4]. We compute $C_7(\mu_b)$ and $C'_7(\mu_b)$ at LO in

the MSSM with QFV and study the deviation of the MSSM predictions from their SM ones.[2] Following the standard procedure, first we compute $C_{7,8}(\mu_W)$ and $C'_{7,8}(\mu_W)$ at the weak scale μ_W at LO in the MSSM and then we compute $C_7(\mu_b)$ and $C'_7(\mu_b)$ by using the QCD RGEs for the scale evolution at leading log (LL) level [8][3]:

$$C_7(\mu_b) = \eta^{\frac{16}{23}} C_7(\mu_W) + \frac{8}{3}(\eta^{\frac{14}{23}} - \eta^{\frac{16}{23}}) C_8(\mu_W) + \sum_{i=1}^{8} h_i \eta^{a_i} C_2(\mu_W)$$
$$C'_7(\mu_b) = \eta^{\frac{16}{23}} C'_7(\mu_W) + \frac{8}{3}(\eta^{\frac{14}{23}} - \eta^{\frac{16}{23}}) C'_8(\mu_W) + \sum_{i=1}^{8} h_i \eta^{a_i} C'_2(\mu_W), \tag{10}$$

where

$$\eta = \alpha_s(\mu_W)/\alpha_s(\mu_b)$$
$$h_i = \left(\frac{626126}{272277}, -\frac{56281}{51730}, -\frac{3}{7}, -\frac{1}{14}, -0.6494, -0.0380, -0.0186, -0.0057\right)$$
$$a_i = \left(\frac{14}{23}, \frac{16}{23}, \frac{6}{23}, -\frac{12}{23}, 0.4086, -0.4230, -0.8994, 0.1456\right). \tag{11}$$

We take the NLO formula with 5 flavors for the strong coupling constant $\alpha_s(\mu)$ for $\mu_b \lesssim \mu \lesssim \mu_W$ [8]:

$$\alpha_s(\mu) = \frac{\alpha_s(m_Z)}{v(\mu)}\left[1 - \frac{\beta_1}{\beta_0}\frac{\alpha_s(m_Z)}{4\pi}\frac{\ln v(\mu)}{v(\mu)}\right], \tag{12}$$

where

$$v(\mu) = 1 - \beta_0 \frac{\alpha_s(m_Z)}{2\pi}\ln\left(\frac{m_Z}{\mu}\right), \tag{13}$$

$\beta_0 = \frac{23}{3}$, $\beta_1 = \frac{116}{3}$ and m_Z is the Z boson mass. We take $m_Z = 91.2$ GeV and $\alpha_s(m_Z) = 0.1179$ [24]. The SM and MSSM contribution to $C_2(\mu_W) = C_2^{\rm SM}(\mu_W) + C_2^{\rm MSSM}(\mu_W)$ is 1 and 0 at LO, respectively. The SM and MSSM contributions to $C'_2(\mu_W) = C'^{\rm SM}_2(\mu_W) + C'^{\rm MSSM}_2(\mu_W)$ are 0 at LO. In our numerical analysis, we take $\mu_W = 160$ GeV and $\mu_b = 4.8$ GeV [3].

We use the numerical results for $C^{(\prime)}_{7,8}(\mu_W)$ at LO in the MSSM obtained from the public code SPheno-v3.3.8 [26,27], which takes into account the following one-loop contributions to $C^{(\prime)}_{7,8}(\mu_W)$ at the weak scale μ_W (see Fig. 1):

(1) SM one-loop contributions:
  up-type quark—W^+ loops
(2) MSSM one-loop contributions:
  up-type squark-chargino loops
  down-type squark-gluino loops
  down-type squark-neutralino loops
  up-type quark—H^+ loops

Here the chargino $\tilde{\chi}^{\pm}_{1,2}$ is a mixture of charged wino $\tilde{W}^{\pm}$ and charged higgsino $\tilde{H}^{\pm}$, the neutralino $\tilde{\chi}^0_{1,2,3,4}$ is a mixture

[2]Here it is worth to mention that these WCs are related to the photon polarization in radiative B-meson decays. The helicity polarization of the external photon in $b \to s\gamma$ is defined as

$$P(b \to s\gamma) \equiv \frac{B(b \to s\gamma_R) - B(b \to s\gamma_L)}{B(b \to s\gamma_R) + B(b \to s\gamma_L)}. \tag{8}$$

At LO it is given as [18]

$$P(b \to s\gamma) = \frac{|C'_7(\mu_b)|^2 - |C_7(\mu_b)|^2}{|C'_7(\mu_b)|^2 + |C_7(\mu_b)|^2}. \tag{9}$$

In the SM $C'_7(\mu_b)$ is strongly suppressed by a factor m_s/m_b and hence the photon in $b \to s\gamma$ decay is predominantly left-handed. In principle, the photon polarization can be extracted from the measurement of radiative B-meson decays in the experiments such as Belle II and LHCb Upgrade [1,2,29–38].

[3]Here we comment on the RG running of the WCs at LL level. In footnote 5 of Ref. [18], it is argued as follows: In Ref. [39] it has been pointed out that the gluino contribution to the WCs $C^{(\prime)}_{7,8}(\mu)$ is the sum of two different pieces, one proportional to the gluino mass and one proportional to the bottom mass, which have a different RG evolution (i.e., Eqs. (40) and (41) of [39], respectively). However, it has been found that at LO this is equivalent to the usual SM RG-evolution (i.e., Eqs. (13,14) of [18] which correspond to Eq. (10) of the present paper) once the running bottom mass $m_b(\mu_0)$ is used instead of the pole mass m_b(pole) in the WCs $C^{(\prime)}_i(\mu_0)$, where μ_0 is the high-energy matching scale (e.g., the electroweak scale μ_W). We have also confirmed this point (fact) independently of Ref. [18]. Here, note that we have used the public code SPheno-v3.3.8 [26,27] in the computation of the WCs $C^{(\prime)}_{7,8}(\mu_0 = 160$ GeV), and that SPheno-v3.3.8 uses the running b-quark mass $m_b(\mu_0 = 160$ GeV) (*not* the pole mass m_b(pole)) in the computation of the $C^{(\prime)}_{7,8}(\mu_0 = 160$ GeV). Therefore, Eqs. (40) and (41) of [39] are equivalent to the usual SM RG-evolution (i.e., Eq. (10) of the present paper) at LO. Moreover, just after Eq. (41) in Ref. [39] it is clearly stated that the terms $R_{7b,\tilde{g}}(\mu_b)$ and $R_{8b,\tilde{g}}(\mu_b)$ turn out to be numerically very small with respect to the other terms on the right-hand sides of Eq. (41) for the RG running of the WCs. Here $R_{7b,\tilde{g}}(\mu_b)$ and $R_{8b,\tilde{g}}(\mu_b)$ are linear combinations of the WCs (such as $C^b_{i,\tilde{g}}(\mu_W)$ (i = 15, 16, 19, 20)) of the additional four-quark operators in Eq. (15) of [39], all of which are operators at NLO of QCD. Hence, the effects of the additional four-quark operators onto the RG running of $C^{(\prime)}_{7,8}(\mu)$ are numerically very small. Therefore, the contributions of the WCs of the new four-quark operators mentioned in [39] (which are all at NLO of QCD) to the RG scale evolution (RG running) are numerically very small and hence the presence of the mentioned new four-quark operators *cannot* change Eq. (10) in the present paper practically (essentially).

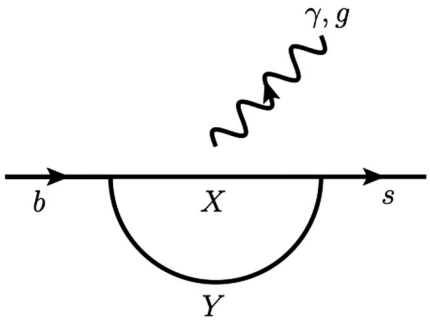

FIG. 1. The SM and MSSM one-loop contributions to the WCs $C_{7,8}(\mu_W)$ and $C'_{7,8}(\mu_W)$ at the weak scale μ_W for the transitions $b_R \to s_L\gamma_L, g_L$ and $b_L \to s_R\gamma_R, g_R$, respectively [see Eqs. (5)–(7)]. Here γ_L, g_L and γ_R, g_R are left-handed photon, gluon and right-handed photon, gluon, respectively. The photon is emitted from any electrically charged line and the gluon from any color charged line. For the SM one-loop contributions $(\mathrm{X},\mathrm{Y}) = (\mathrm{t/c/u}, W^+)$. For the MSSM one-loop contributions $(\mathrm{X},\mathrm{Y}) = (\mathrm{stop/scharm/sup,chargino})$, (sbottom/sstrange/sdown, gluino), (sbottom/sstrange/sdown, neutralino) and (t/c/u, H^+), where stop/scharm/sup denotes top-, charm-, up-squark mixtures and so on.

of photino $\tilde{\gamma}$, zino $\tilde{Z}$ and two neutral higgsinos $\tilde{H}^0_{1,2}$, and H^+ is the charged Higgs boson.

Before we show the results of the full parameter scan, we comment on the expected qualitative behavior of the MSSM one-loop contributions to $C_7^{(\prime)}(\mu_b)$ at the bottom mass scale μ_b. We find that large squark trilinear couplings $T_{U23,32,33}, T_{D23,32,33}$, large $M^2_{Q23}, M^2_{U23}, M^2_{D23}$, large bottom Yukawa coupling Y_b for large $\tan\beta$, and large top Yukawa coupling Y_t can lead to large MSSM one-loop contributions to $C_{7,8}^{(\prime)}(\mu_W)$ at the weak scale μ_W, which results in large MSSM one-loop contributions to $C_7^{(\prime)}(\mu_b)$ at the bottom mass scale μ_b [see Eq. (10)]. This is mainly due to the following reasons:

(i) The lighter up-type squarks $\tilde{u}_{1,2,3}$ are strong $\tilde{c}_{L,R} - \tilde{t}_{L,R}$ mixtures for large M^2_{Q23}, M^2_{U23}, $T_{U23,32,33}$. The lighter down-type squarks $\tilde{d}_{1,2,3}$ are strong $\tilde{s}_{L,R} - \tilde{b}_{L,R}$ mixtures for large M^2_{Q23}, M^2_{D23}, $T_{D23,32,33}$. Here note that $|T_{U23,32,33}|$ can be large due to large Y_t [see Eqs. (A1), (A3)] and that $|T_{D23,32,33}|$ can be large due to large Y_b for large $\tan\beta$ [see Eqs. (A2), (A4)]. In the following we assume these setups.

(ii) As for the up-type squark-chargino loop contributions to $C_7(\mu_W)$ and $C_8(\mu_W)$ which is the effective coupling for the transition $b_R \to s_L\gamma$ and $b_R \to s_L g$, respectively; The $b_R - \tilde{u}_{1,2,3} - \tilde{\chi}^{\pm}_{1,2}$ vertex which contains the $b_R - \tilde{t}_L - \tilde{H}^{\pm}$ coupling can be enhanced by the large bottom Yukawa coupling Y_b for large $\tan\beta$. The $s_L - \tilde{u}_{1,2,3} - \tilde{\chi}^{\pm}_{1,2}$ vertex contains the $s_L - \tilde{c}_L - \tilde{W}^{\pm}$ coupling which is not CKM-suppressed.[4] This vertex contains also the s_L-$\tilde{t}_R$-$\tilde{H}^{\pm}$ coupling which is enhanced by the large top Yukawa coupling Y_t despite the suppression due to the CKM factor V^*_{ts}. Hence, the up-type squark-chargino loop contributions to $C_{7,8}(\mu_W)$ can be enhanced by the large Y_b for large $\tan\beta$ and the large Y_t, and further by the large $\tilde{c}_L$-$\tilde{t}_L$ mixing term M^2_{Q23} and the large $\tilde{t}_L$-$\tilde{t}_R$ mixing term T_{U33} for which $\tilde{u}_{1,2,3}$ contain a strong mixture of $\tilde{c}_L$, $\tilde{t}_L$ and $\tilde{t}_R$. Important parts of this squark-chargino loop contributions to $C_{7,8}(\mu_W)$ are schematically illustrated in terms of the mass-insertion approximation in Fig. 2.

(iii) As for the down-type squark-gluino loop contributions to $C_{7,8}(\mu_W)$; The b_R-$\tilde{d}_{1,2,3}$-$\tilde{g}$ vertex which contains the b_R-$\tilde{b}_R$-$\tilde{g}$ coupling can be enhanced by the sizable QCD coupling. The s_L-$\tilde{d}_{1,2,3}$-$\tilde{g}$ vertex which contains the s_L-$\tilde{s}_L$-$\tilde{g}$ coupling can also be enhanced by the QCD coupling. Furthermore, absence of the CKM-suppression factor in this loop diagram results in additional strong enhancement. Therefore, the down-type squark-gluino loop contributions to $C_{7,8}(\mu_W)$ can be enhanced by the sizable QCD coupling, and further by the large $\tilde{b}_R$-$\tilde{s}_L$ mixing term T_{D32} for which $\tilde{d}_{1,2,3}$ contain a strong mixture of $\tilde{b}_R$ and $\tilde{s}_L$. Moreover, $|T_{D32}|$ can be large due to large Y_b for large $\tan\beta$ [see Eq. (A4)]. An important part of this squark-gluino loop contribution to $C_{7,8}(\mu_W)$ is schematically illustrated in terms of the mass-insertion approximation in Fig. 3(a).

(iv) As for the down-type squark-neutralino loop contributions to $C_{7,8}(\mu_W)$; The b_R-$\tilde{d}_{1,2,3}$-$\tilde{\chi}^0_{1,2,3,4}$ vertex which contains the b_R-$\tilde{b}_R$-$\tilde{\gamma}/\tilde{Z}$ and b_R-$\tilde{b}_L$-$\tilde{H}^0_1$ couplings with the latter coupling being proportional to Y_b can be enhanced by large Y_b for large $\tan\beta$. The s_L-$\tilde{d}_{1,2,3}$-$\tilde{\chi}^0_{1,2,3,4}$ vertex contains the s_L-$\tilde{s}_L$-$\tilde{\gamma}/\tilde{Z}$ couplings. The absence of the CKM-suppression factor in this loop diagram results in additional strong enhancement. Hence, the down-type squark-neutralino loop contributions to $C_{7,8}(\mu_W)$ can be enhanced by large Y_b for large $\tan\beta$, and further by the large $\tilde{b}_R$-$\tilde{s}_L$ and $\tilde{b}_L$-$\tilde{s}_L$ mixing terms (T_{D32} and M^2_{Q23}), for which $\tilde{d}_{1,2,3}$ contain a strong mixture of $\tilde{b}_R$-$\tilde{s}_L$ and $\tilde{b}_L$-$\tilde{s}_L$. Moreover, $|T_{D32}|$ controlled by Y_b can be large for large $\tan\beta$ [see Eq. (A4)].

(v) As for the up-type quark—H^+ loop contributions to $C_{7,8}(\mu_W)$; The b_R-t-H^+ vertex which contains the b_R-t_L-H^+ coupling can be enhanced by large Y_b for

[4]Note that the CKM-suppression factor V^*_{ts} is factored out from WCs C_i in their definition [see Eq. (5)]. Therefore, absence of the CKM-suppression factor in the one-loop diagram results in strong enhancement of the loop contribution to the WCs C_i.

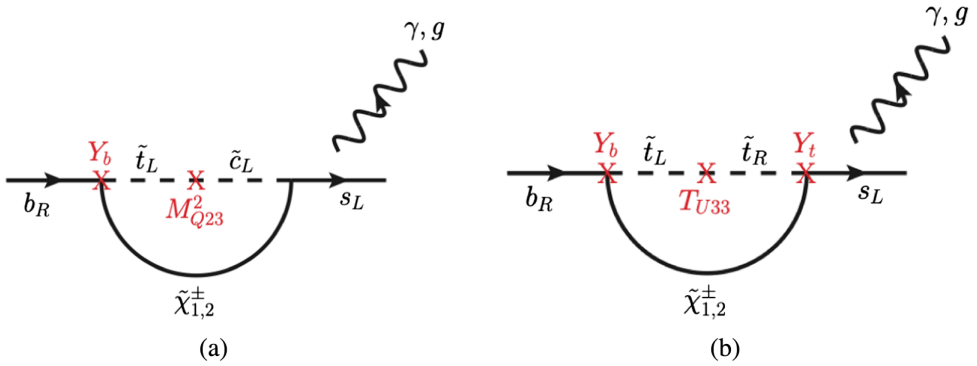

FIG. 2. Schematic illustration of important parts of the up-type squark-chargino loop contributions to $C_{7,8}(\mu_W)$ in terms of the mass-insertion approximation.

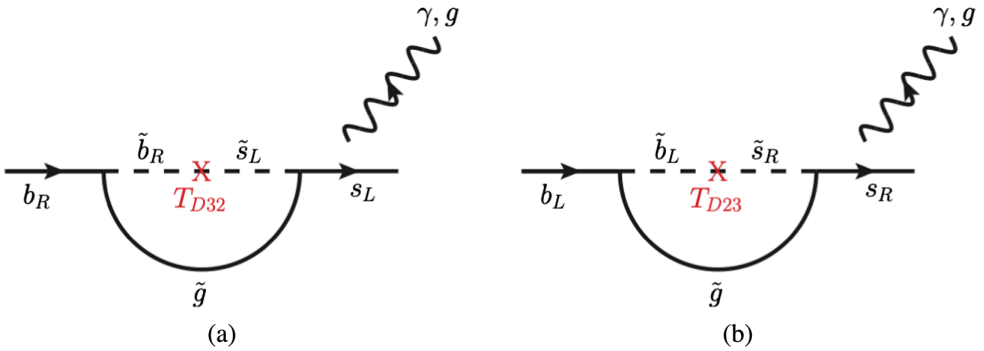

FIG. 3. Schematic illustration of an important part of the down-type squark-gluino loop contributions to (a) $C_{7,8}(\mu_W)$ and (b) $C'_{7,8}(\mu_W)$ in terms of the mass-insertion approximation.

large $\tan\beta$. The s_L-t-H^+ vertex which contains the s_L-t_R-H^+ coupling can be enhanced by the large top-quark Yukawa coupling Y_t despite the suppression due to the CKM factor V^*_{ts}. Hence t-H^+ loop contributions to $C_{7,8}(\mu_W)$ can be enhanced by large Y_b for large $\tan\beta$ and large Y_t. The top quark—H^+ loop contribution to $C_{7,8}(\mu_W)$ is schematically illustrated in Fig. 4.

(vi) As for the up-type squark-chargino loop contributions to $C'_7(\mu_W)$ and $C'_8(\mu_W)$ which are the effective couplings for the transition $b_L \to s_R\gamma$ and $b_L \to s_R g$, respectively; From a similar argument one finds that these loop contributions to $C'_{7,8}(\mu_W)$ should be small due to the very small s-quark Yukawa coupling Y_s.

(vii) As for the down-type squark-gluino loop contributions to $C'_{7,8}(\mu_W)$; The b_L-$\tilde{d}_{1,2,3}$-$\tilde{g}$ vertex which contains the b_L-$\tilde{b}_L$-$\tilde{g}$ coupling can be enhanced by the sizable QCD coupling. The s_R-$\tilde{d}_{1,2,3}$-$\tilde{g}$ vertex which contains the s_R-$\tilde{s}_R$-$\tilde{g}$ coupling can also be enhanced by the QCD coupling. Absence of the CKM-suppression factor in this loop diagram results in additional strong enhancement. Therefore, the down-type squark-gluino loop contributions to $C'_{7,8}(\mu_W)$ can be enhanced by the sizable QCD couplings, and further by large $\tilde{b}_L$-$\tilde{s}_R$ mixing term T_{D23} for which $\tilde{d}_{1,2,3}$ contain a strong mixture of $\tilde{b}_L$ and $\tilde{s}_R$. Moreover, $|T_{D23}|$ can be large due to large Y_b for large $\tan\beta$ [see Eq. (A4)]. An important part of this squark-gluino loop contribution to $C'_{7,8}(\mu_W)$ is schematically illustrated in terms of the mass-insertion approximation in Fig. 3(b).

(viii) As for the down-type squark-neutralino loop contributions to $C'_{7,8}(\mu_W)$; The b_L-$\tilde{d}_{1,2,3}$-$\tilde{\chi}^0_{1,2,3,4}$ vertex which contains the b_L-$\tilde{b}_L$-$\tilde{\gamma}/\tilde{Z}$ and b_L-$\tilde{b}_R$-$\tilde{H}^0_1$ couplings with the latter coupling being proportional to

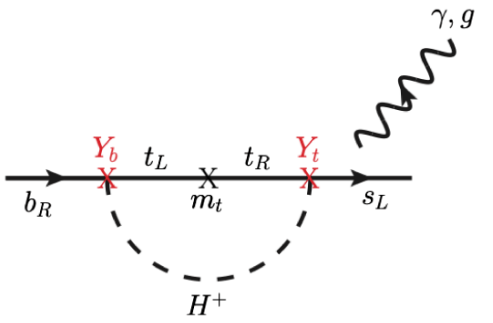

FIG. 4. Schematic illustration of the top quark—H^+ loop contribution to $C_{7,8}(\mu_W)$.

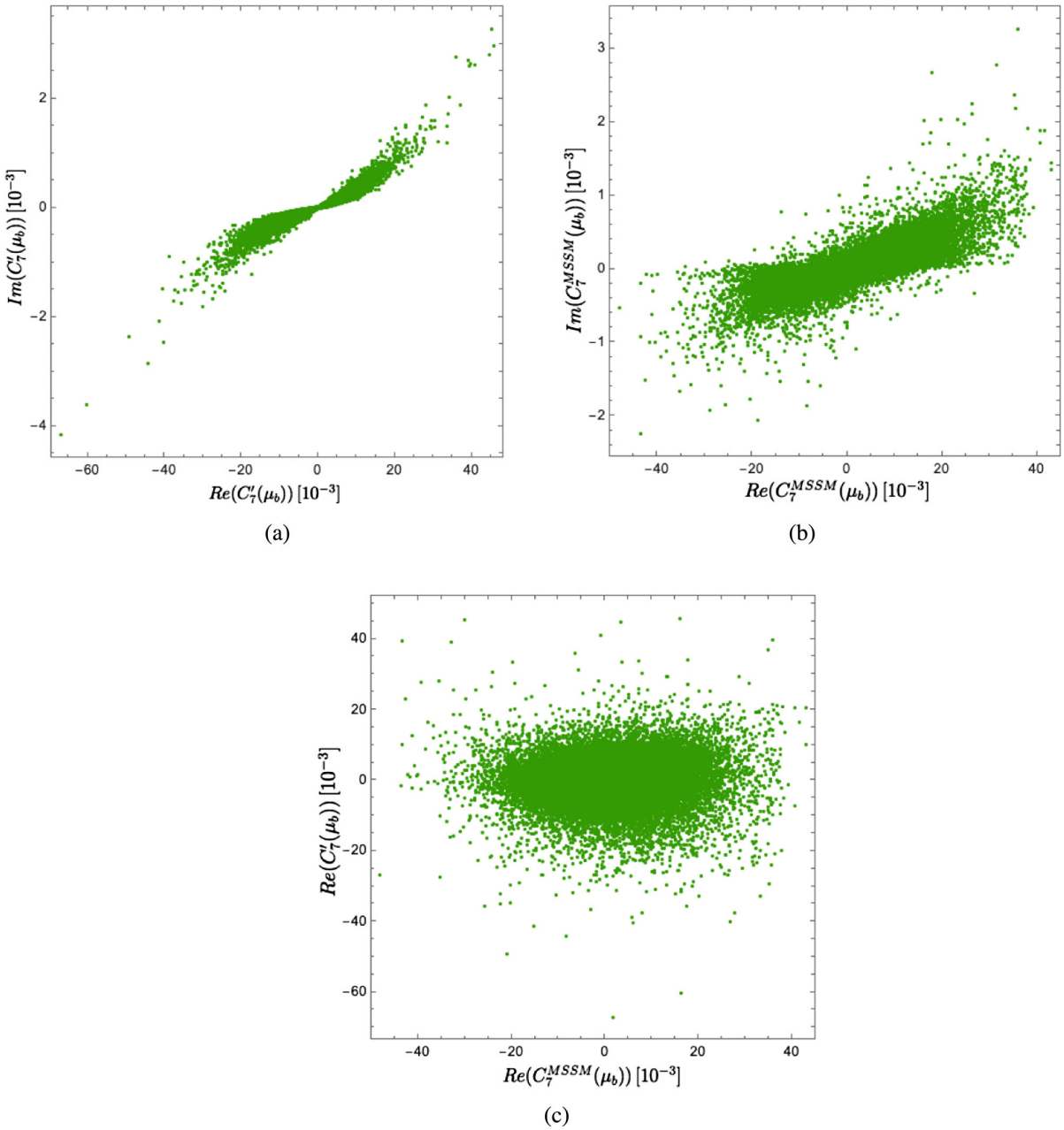

FIG. 5. The scatter plot of the scanned parameter points within the ranges given in Table I in the planes of (a) $\mathrm{Re}(C_7'(\mu_b))$-$\mathrm{Im}(C_7'(\mu_b))$, (b) $\mathrm{Re}(C_7^{\mathrm{MSSM}}(\mu_b))$-$\mathrm{Im}(C_7^{\mathrm{MSSM}}(\mu_b))$, and (c) $\mathrm{Re}(C_7^{\mathrm{MSSM}}(\mu_b))$-$\mathrm{Re}(C_7'(\mu_b))$.

Y_b can be enhanced by large Y_b for large $\tan\beta$. The s_R-$\tilde{d}_{1,2,3}$-$\tilde{\chi}^0_{1,2,3,4}$ vertex contains the s_R-$\tilde{s}_R$-$\tilde{\gamma}/\tilde{Z}$ coupling. Absence of the CKM-suppression factor in this loop diagram results in additional strong enhancement. Hence, the down-type squark-neutralino loop contributions to $C'_{7,8}(\mu_W)$ can be enhanced by large Y_b for large $\tan\beta$, and further by large $\tilde{b}_L$-$\tilde{s}_R$ and $\tilde{b}_R$-$\tilde{s}_R$ mixing terms T_{D23} and M^2_{D23}, for which $\tilde{d}_{1,2,3}$ contain strong mixtures of $\tilde{b}_L$-$\tilde{s}_R$ and $\tilde{b}_R$-$\tilde{s}_R$. Moreover, $|T_{D23}|$ controlled by Y_b can be large for large $\tan\beta$ [see Eq. (A4)].

(ix) As for the up-type quark—H^+ loop contributions to $C'_{7,8}(\mu_W)$; These contributions turn out to be very small due to the very small Y_s.

In the following we will show scatter plots in various planes obtained from the MSSM parameter scan described above (see Table I), respecting all the relevant constraints (see Appendix A).

In Fig. 5 we show scatter plots for $C_7^{\mathrm{MSSM}}(\mu_b)$ and $C_7'(\mu_b)$. In Fig. 5(a) we show a scatter plot in the $\mathrm{Re}(C_7'(\mu_b))$-$\mathrm{Im}(C_7'(\mu_b))$ plane. We see that the MSSM contribution to $\mathrm{Re}(C_7'(\mu_b))$ can be as large as ~ -0.07, which could correspond to an about 4σ New Physics (NP)

signal significance in the combination of the future LHCb Upgrade (Phase III) and Belle II (Phase II) experiments (see Fig. A. 13 of [3]). Note that $|\mathrm{Im}(C_7'(\mu_b))|$ is very small ($\lesssim 0.004$) and that $C_7'(\mu_b) \simeq 0$ in the SM.

In Fig. 5(b) we show the scatter plot in the $\mathrm{Re}(C_7^{\mathrm{MSSM}}(\mu_b))$-$\mathrm{Im}(C_7^{\mathrm{MSSM}}(\mu_b))$ plane. We see that the MSSM contribution to $\mathrm{Re}(C_7(\mu_b))$ can be as large as ~ -0.05, which could correspond to an about 3σ NP signal significance in the combination of the future LHCb Upgrade (50 fb^{-1}) and Belle II (50 ab^{-1}) experiments (see Fig. 8 of [3]). Note that $|\mathrm{Im}(C_7^{\mathrm{MSSM}}(\mu_b))|$ is very small ($\lesssim 0.003$) and that the MSSM contribution $C_7^{\mathrm{MSSM}}(\mu_b)$ can be quite sizable compared to $C_7^{\mathrm{SM}}(\mu_b) \simeq -0.325$.

In Fig. 5(c) we show a scatter plot in the $\mathrm{Re}(C_7^{\mathrm{MSSM}}(\mu_b))$-$\mathrm{Re}(C_7'(\mu_b))$ plane. We see that the $\mathrm{Re}(C_7'(\mu_b))$ and $\mathrm{Re}(C_7^{\mathrm{MSSM}}(\mu_b))$ can be quite sizable simultaneously.

Here we comment on the errors of the data on $C_7'(\mu_b)$ and $C_7^{NP}(\mu_b)$. The errors of the data on $C_7'(\mu_b)$ and $C_7^{NP}(\mu_b) \equiv C_7(\mu_b) - C_7^{\mathrm{SM}}(\mu_b)$ from the future B-meson experiments shown in Figs. A.13 and 8 of [3] stem from experimental and theoretical errors. In general, B-meson observables are functions of the relevant WCs such as $C_7'(\mu_b)$ and $C_7(\mu_b)$. Hence, from the observed data on relevant B-meson observables one can determine (extract) the values of the WCs. The WCs thus determined (extracted) have two types of errors, one is the experimental error stemming from the (systematic and statistical) errors of the observable data and the other is the theoretical error due to the uncertainties of input parameters, such as the CKM matrix elements ($V_{ts}, V_{tb}\ldots$), hadronic form factors and meson-decay constants, in the computation (prediction) of the observables by using the WCs (i.e., the effective couplings).

Here we remark the following points: (i) As for the determination of $C_7(\mu_b)$ one can get much more precise information from the fully inclusive $B(B \to X_s\gamma)$ measurement than from the measurement of the exclusive observables such as $B(B \to K^*\gamma)$[5] since the theoretical predictions for the exclusive observables involve hadronic form factors which have large theoretical uncertainties. (ii) The fully inclusive observable $B(B \to X_s\gamma)$ can be measured reliably and precisely at Belle II [1] whereas its measurement is very difficult at LHCb [2]. (iii) As a result, Belle II plays a specially important role in the precise determination (extraction) of $C_7(\mu_b)$ in the near future.

As for the experimental errors of the WCs $C_7'(\mu_b)$ and $C_7^{NP}(\mu_b)$ obtained (extracted) from the future B-meson experiments, Belle II is now planning to upgrade to accumulate about 5 times larger data (up to $\sim$250 ab^{-1}) [40]. If this is realized, the (statistical) uncertainty of the observable data from Belle II could be reduced by a factor of about $\sqrt{5}$.

As for the theoretical errors of the WCs $C_7'(\mu_b)$ and $C_7^{NP}(\mu_b)$ obtained (extracted) from the B-meson experiments, there is a sign of promising possibility of significant reduction of the theoretical errors in the future: Very recently M. Misiak *et al.* performed a new computation of $B(B \to X_s\gamma)$ in the SM at the NNLO in QCD [12]. Taking into account the recently improved estimates of nonperturbative contributions, they have obtained $B(B \to X_s\gamma) = (3.40 \pm 0.17) \times 10^{-4}$ for $E_\gamma > 1.6$ GeV. Compared with their previous SM prediction $B(B \to X_s\gamma) = (3.36 \pm 0.23) \times 10^{-4}$ [11], the theoretical uncertainty is now reduced from 6.8% to 5.0%. Note here that the Figs. A.13 and 8 of [3] showing expected errors of $C_7'(\mu_b)$ and $C_7^{NP}(\mu_b)$ obtained (extracted) from the future B-meson experiments were made in the year 2017.

Hence, in case the significant reduction of the experimental and theoretical errors is achieved in the future, the NP signal significances for $\mathrm{Re}(C_7'(\mu_b))$ and $\mathrm{Re}(C_7^{\mathrm{NP}}(\mu_b))$ in the MSSM could be significantly higher than those mentioned above which are about 4σ NP significances for $\mathrm{Re}(C_7'(\mu_b))$ and about 3σ significance for $\mathrm{Re}(C_7^{\mathrm{MSSM}}(\mu_b))$.

Thus, it is very important to improve the precision of both theory and experiment on B-meson physics by a factor about 1.5 or so in view of NP search (such as SUSY search). Therefore, we strongly encourage theorists and experimentalists to challenge this task.

In Fig. 6 we show scatter plots in the T_{U23}-$\mathrm{Re}(C_7'(\mu_b))$, T_{U32}-$\mathrm{Re}(C_7'(\mu_b))$, T_{U33}-$\mathrm{Re}(C_7'(\mu_b))$ and $\tan\beta$-$\mathrm{Re}(C_7'(\mu_b))$ planes. From Fig. 6(a) we see that $\mathrm{Re}(C_7'(\mu_b)) \simeq \mathrm{Re}(C_7'^{\mathrm{MSSM}}(\mu_b))$ can be sizable ($-0.07 \lesssim \mathrm{Re}(C_7'(\mu_b)) \lesssim 0.05$) for large T_{U23} ($\gtrsim$3 TeV). From Fig. 6(b) we see that $\mathrm{Re}(C_7'(\mu_b))$ can be large for large $|T_{U32}|$: $-0.07 \lesssim \mathrm{Re}(C_7'(\mu_b)) \lesssim 0.025$ for $T_{U32} \lesssim -2$ TeV and $-0.04 \lesssim \mathrm{Re}(C_7'(\mu_b)) \lesssim 0.045$ for $T_{U32} \gtrsim 2$ TeV. A significant correlation between $\mathrm{Re}(C_7'(\mu_b))$ and T_{U32} can be seen. From Fig. 6(c) we see that $\mathrm{Re}(C_7'(\mu_b))$ can be large for large $|T_{U33}| \gtrsim 3$ TeV. The fewer scatter points around $T_{U33} = 3.5$ TeV is due to the fact that the m_{h^0} bound tends to be violated around this point. From Fig. 6(d) we see that $\mathrm{Re}(C_7'(\mu_b))$ can be large for large $\tan\beta$: $-0.07 \lesssim \mathrm{Re}(C_7'(\mu_b)) \lesssim 0.05$ for $\tan\beta \gtrsim 40$. All of these features are consistent with our expectation from the argument above.

In Fig. 7 we show scatter plots in the T_{D23}-$\mathrm{Re}(C_7'(\mu_b))$, T_{D32}-$\mathrm{Re}(C_7'(\mu_b))$ and T_{D33}-$\mathrm{Re}(C_7'(\mu_b))$ planes. From Figs. 7(a) and 7(b) we see that $\mathrm{Re}(C_7'(\mu_b)) \simeq \mathrm{Re}(C_7'^{\mathrm{MSSM}}(\mu_b))$ can be large ($-0.07 \lesssim \mathrm{Re}(C_7'(\mu_b)) \lesssim 0.05$) for large T_{D23}, T_{D32} ($\lesssim -1.5$ TeV). An appreciable correlation between T_{D23} and $\mathrm{Re}(C_7'(\mu_b))$ can be seen in Fig. 7(a). From Fig. 7(b) we see that it can be large for large $|T_{D33}| \gtrsim 2$ TeV. These behaviors are also consistent with our expectation.

[5]Here note that $B(B \to X_s\gamma) \simeq B(b \to s\gamma)$ is proportional to $|C_7(\mu_b)|^2 + |C_7'(\mu_b)|^2$ at LO.

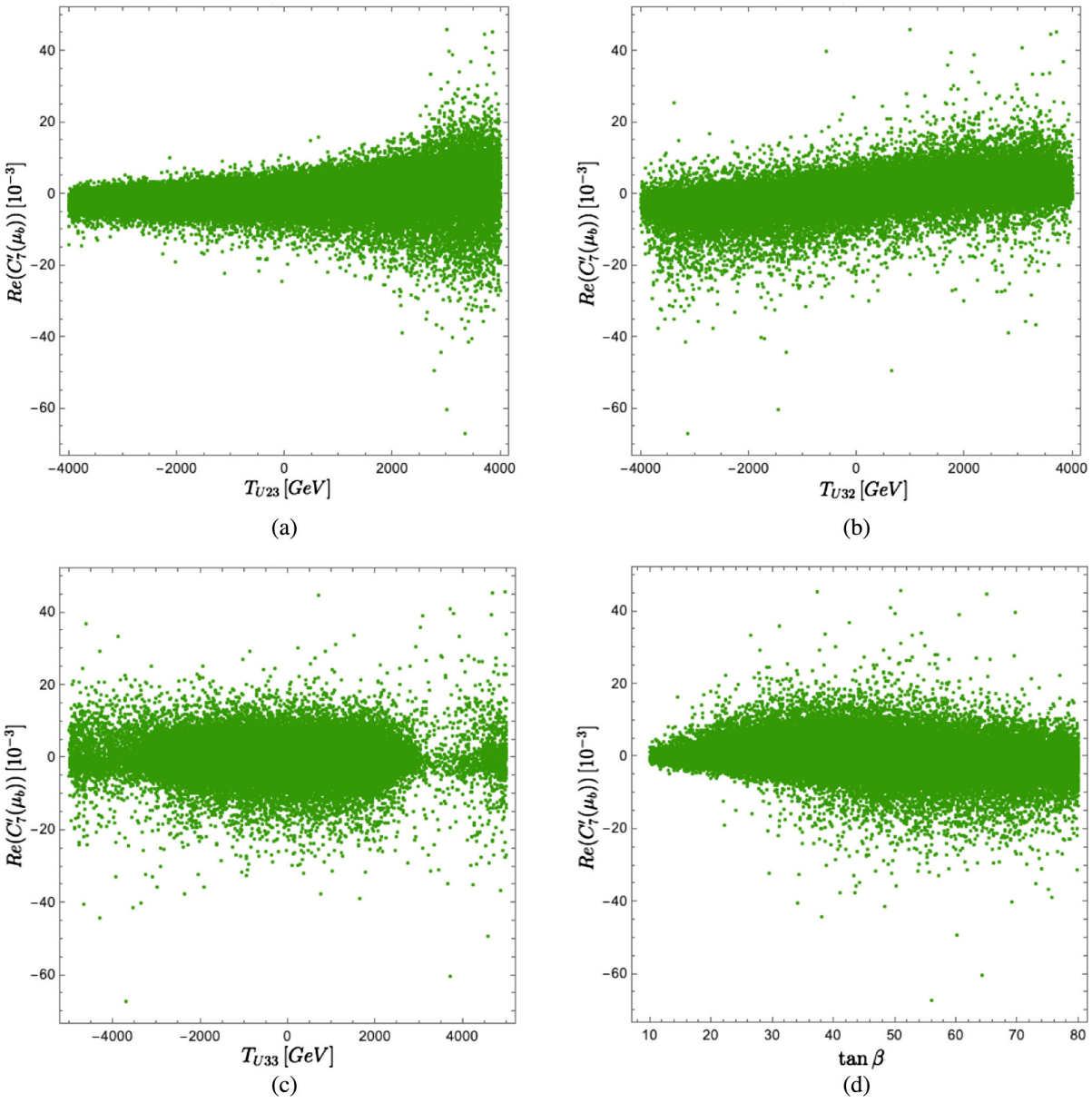

FIG. 6. The scatter plots of the scanned parameter points within the ranges given in Table I in the planes of (a) T_{U23}-Re$(C_7'(\mu_b))$, (b) T_{U32}-Re$(C_7'(\mu_b))$, (c) T_{U33}-Re$(C_7'(\mu_b))$ and (d) tanβ-Re$(C_7'(\mu_b))$.

In Fig. 8 we show scatter plots in the planes of $T_{U23}-\mathrm{Re}(C_7^{\mathrm{MSSM}}(\mu_b))$, T_{U32}-Re$(C_7^{\mathrm{MSSM}}(\mu_b))$, T_{U33}-Re$(C_7^{\mathrm{MSSM}}(\mu_b))$ and tanβ-Re$(C_7^{\mathrm{MSSM}}(\mu_b))$. From Figs. 8(a) and 8(b) we see that Re$(C_7^{\mathrm{MSSM}}(\mu_b))$ can be sizable (up to $\sim\pm 0.05$) compared with Re$(C_7^{\mathrm{SM}}(\mu_b))\simeq -0.325$ for large T_{U23} and $T_{U32}(\gtrsim 2$ TeV). From Fig. 8(c) we see that it can be large for large $|T_{U33}|$: $-0.03\lesssim \mathrm{Re}(C_7^{\mathrm{MSSM}}(\mu_b))\lesssim 0.045$ for $T_{U33}\lesssim -2$ TeV and $-0.05\lesssim \mathrm{Re}(C_7^{\mathrm{MSSM}}(\mu_b))\lesssim 0.035$ for $T_{U33}\gtrsim 2$ TeV. There is a significant correlation between Re$(C_7^{\mathrm{MSSM}}(\mu_b))$ and T_{U33}, which can be explained partly by the important contribution of Fig. 2(b) [see Eq. (10)]. The fewer scatter points around $T_{U33}=3.5$ TeV is again due to the fact that the m_{h^0} bound tends to be violated around this point. From Fig. 8(d) we see that it can be large (up to $\sim\pm 0.05$) for large tanβ ($\gtrsim$40). These behaviors are also consistent with our expectation.

In Fig. 9 we show scatter plots in the T_{D23}-Re$(C_7^{\mathrm{MSSM}}(\mu_b))$ plane. We see Re$(C_7^{\mathrm{MSSM}}(\mu_b))$ can be sizable (up to $\sim\pm 0.05$) for any values of T_{D23}. We have found that scatter plots in the T_{D32}-Re$(C_7^{\mathrm{MSSM}}(\mu_b))$ and T_{D33}-Re$(C_7^{\mathrm{MSSM}}(\mu_b))$ planes have similar behavior to that in the T_{D23}-Re$(C_7^{\mathrm{MSSM}}(\mu_b))$ plane.

In order to see the relevant parameter dependences of Re$(C_7^{\mathrm{MSSM}}(\mu_b))$ and Re$(C_7'(\mu_b))$ in more detail, we take a reference scenario P1 where we have sizable Re$(C_7^{\mathrm{MSSM}}(\mu_b))$ and Re$(C_7'(\mu_b))$ and then variate the

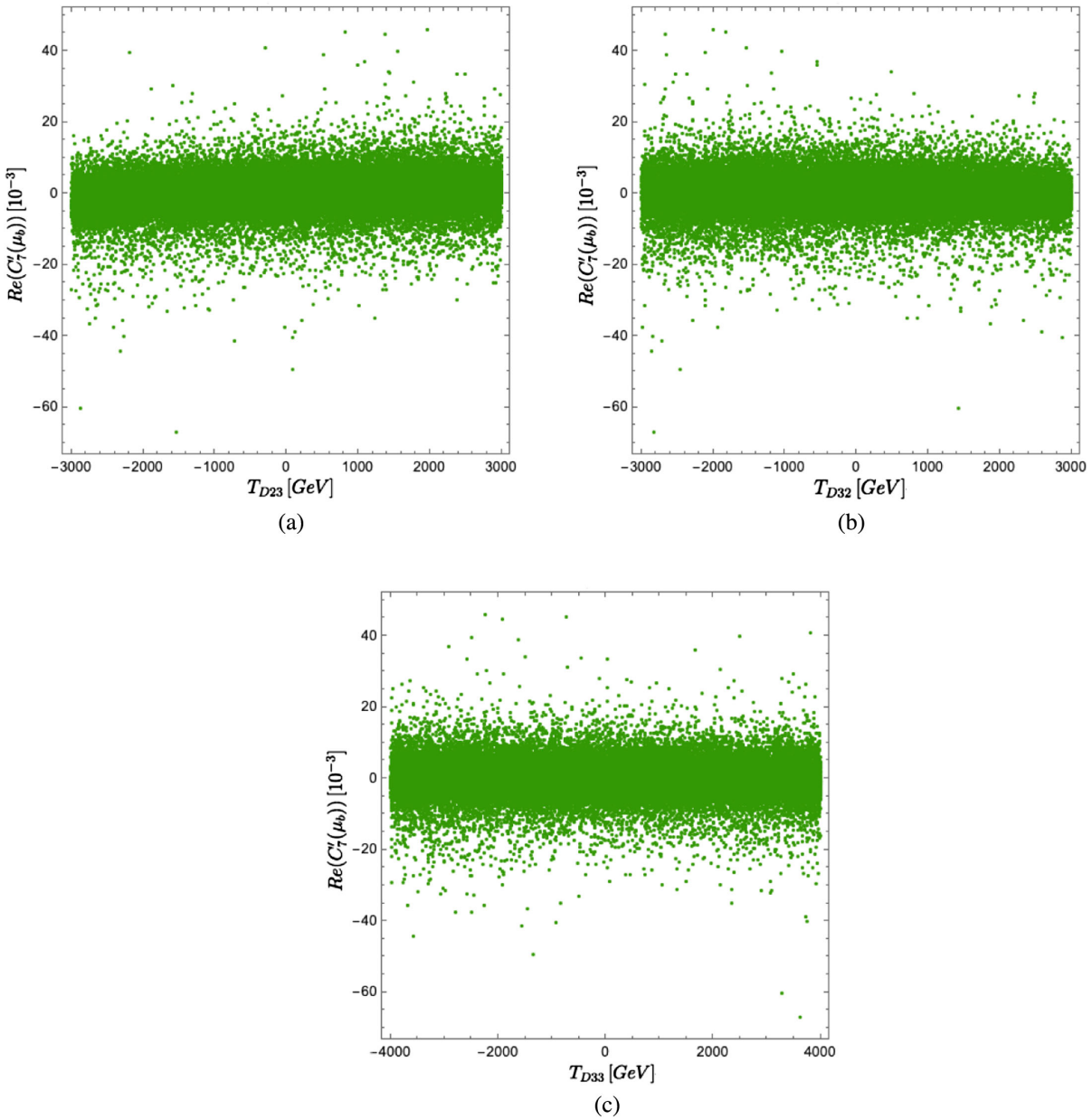

FIG. 7. The scatter plots of the scanned parameter points within the ranges given in Table I in the planes of (a) T_{D23}-Re$(C_7'(\mu_b))$, (b) T_{D32}-Re$(C_7'(\mu_b))$ and (c) T_{D33}-Re$(C_7'(\mu_b))$.

relevant parameters around this point P1. All MSSM input parameters for P1 are shown in Table II, where one has $(\mathrm{Re}(C_7(\mu_b)), \mathrm{Im}(C_7(\mu_b)) = (-0.370, -5.13 \times 10^{-4})$, $(\mathrm{Re}(C_7^{\mathrm{SM}}(\mu_b)), \mathrm{Im}(C_7^{\mathrm{SM}}(\mu_b)) = (-0.325, 5.63 \times 10^{-7})$, $(\mathrm{Re}(C_7^{\mathrm{MSSM}}(\mu_b)), \mathrm{Im}(C_7^{\mathrm{MSSM}}(\mu_b)) = (-0.0441, -5.13 \times 10^{-4})$ and $(\mathrm{Re}(C_7'(\mu_b)), \mathrm{Im}(C_7'(\mu_b)) = (-0.0472, -1.81 \times 10^{-3})$ with $C_7(\mu_b) = C_7^{\mathrm{SM}}(\mu_b) + C_7^{\mathrm{MSSM}}(\mu_b)$.

The scenario P1 satisfies all present experimental and theoretical constraints, see Appendix A. The resulting physical masses of the particles are shown in Table III. The flavor decompositions of the lighter squarks $\tilde{u}_{1,2,3}$ and $\tilde{d}_{1,2,3}$ are shown in Table IV. For the calculation of the masses and the mixing, as well as for the low-energy observables, especially those in the B and K meson sectors (see Table V), we use the public code SPheno v3.3.8 [26,27]. For the calculation of the coupling modifier $\kappa_b = C(h^0 b\bar{b})/C(h^0 b\bar{b})_{\mathrm{SM}}$ (or equivalently the deviation $\mathrm{DEV}(b) \equiv \Gamma(h^0 \to b\bar{b})/\Gamma(h^0 \to b\bar{b})_{\mathrm{SM}} - 1 (= \kappa_b^2 - 1)$ of the width $\Gamma(h^0 \to b\bar{b})$ from its SM value) we compute the width $\Gamma(h^0 \to b\bar{b})$ at full one-loop level in the MSSM with QFV by using the code developed by us [41]. For the coupling modifier $\kappa_x = C(h^0 xx)/C(h^0 xx)_{\mathrm{SM}}$ with $x = g$ or γ (or the deviation $\mathrm{DEV}(x) \equiv \Gamma(h^0 \to xx)/\Gamma(h^0 \to xx)_{\mathrm{SM}} - 1 (= \kappa_x^2 - 1)$) we compute the width $\Gamma(h^0 \to xx)$ according to

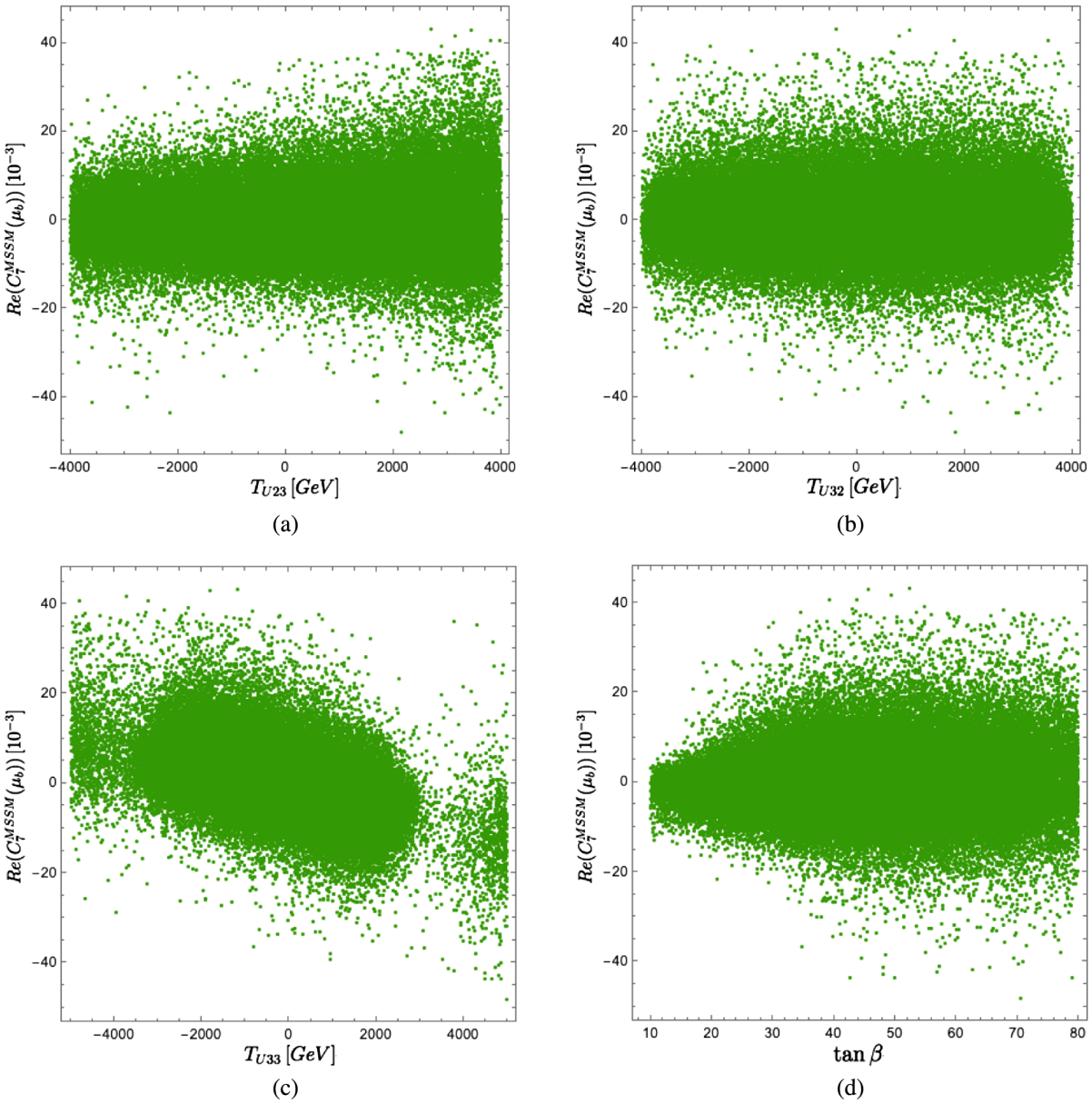

FIG. 8. The scatter plot of the scanned parameter points within the ranges given in Table I in the planes of (a) T_{U23}-Re$(C_7^{\rm MSSM}(\mu_b))$, (b) T_{U32}-Re$(C_7^{\rm MSSM}(\mu_b))$, (c) T_{U33}-Re$(C_7^{\rm MSSM}(\mu_b))$ and (d) $\tan\beta$-Re$(C_7^{\rm MSSM}(\mu_b))$.

[42]. We obtain $\kappa_b = 1.03$ (or DEV$(b) = 0.0686$), $\kappa_g = 0.994$ (or DEV$(g) = -0.0120$) and $\kappa_\gamma = 1.0018$ (or DEV$(\gamma) = 0.0036$), which satisfy the LHC data in Table V. For the B and K meson observables we get; $B(b \to s\gamma) = 3.764 \times 10^{-4}$, $B(b \to sl^+l^-) = 1.589 \times 10^{-6}$, $B(B_s \to \mu^+\mu^-) = 2.5930 \times 10^{-9}$, $B(B^+ \to \tau^+\nu) = 9.942 \times 10^{-5}$, $\Delta M_{B_s} = 17.180[\text{ps}^{-1}]$, $|\epsilon_K| = 2.201 \times 10^{-3}$, $\Delta M_K = 2.304 \times 10^{-15}$ (GeV), $B(K_L^0 \to \pi^0\nu\bar{\nu}) = 2.295 \times 10^{-11}$, and $B(K^+ \to \pi^+\nu\bar{\nu}) = 7.771 \times 10^{-11}$, all of which satisfy the constraints of Table V.

In Figs. 10 and 11 we show contours of Re$(C_7'(\mu_b))$ around the benchmark point P1 in various parameter planes. Figure 10(a) shows contours of Re$(C_7'(\mu_b))$ in the T_{U23}-T_{U32} plane. We see that Re$(C_7'(\mu_b))$ is sensitive to both T_{U23} and T_{U32}, especially to T_{U23}, increases quickly with the increase of T_{U23} and $T_{U32}(< 0)$, as is expected, and can be as large as about -0.07 in the allowed region. We also see that it is large $(-0.07 \lesssim \text{Re}(C_7'(\mu_b)) \lesssim -0.04)$ respecting all the constraints in a significant part of this parameter plane. From Fig. 10(b) we see that Re$(C_7'(\mu_b))$ is also fairly sensitive to T_{U33} and can be as large as ~ -0.08. From Fig. 10(c) we find that Re$(C_7'(\mu_b))$ is very sensitive to $\tan\beta$, especially for large $T_{U23} > 0$, as expected, and can be as large as ~ -0.07. As can be seen in Fig. 10(d), Re$(C_7'(\mu_b))$ is sensitive to M_{U23}^2, especially for large $T_{U23} \gtrsim 2.5$ TeV, as expected, and is large

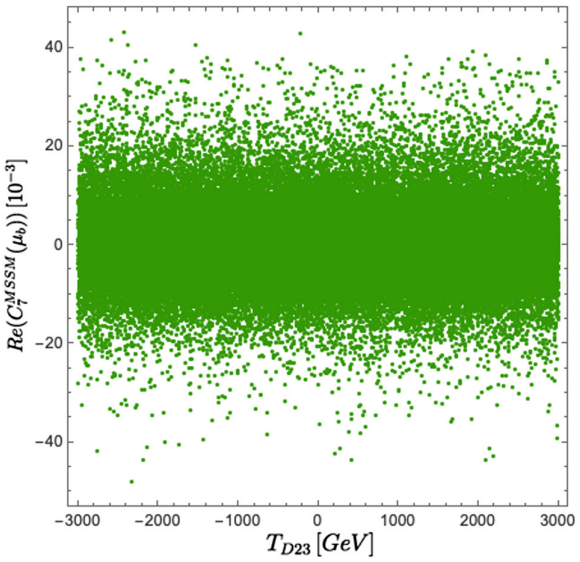

FIG. 9. The scatter plot of the scanned parameter points within the ranges given in Table I in the T_{D23}-$\mathrm{Re}(C_7^{\mathrm{MSSM}}(\mu_b))$ plane.

$(-0.08 \lesssim \mathrm{Re}(C_7'(\mu_b)) \lesssim -0.04)$ respecting all the constraints in a significant part of this parameter plane. Figure 11(a) shows contours of $\mathrm{Re}(C_7'(\mu_b))$ in the T_{D23}-T_{D32} plane. It is fairly sensitive to T_{D23} and mildly dependent on T_{D32} as is expected partly from the contribution of Fig. 3(b) [see Eq. (10)], can be as large as ~ -0.06 in the allowed region, and is large $(-0.058 \lesssim \mathrm{Re}(C_7'(\mu_b)) \lesssim -0.046)$ respecting all the constraints in a significant part of this parameter plane. From Fig. 11(b) we see that $\mathrm{Re}(C_7'(\mu_b))$ is also rather sensitive to T_{D33} and can be as large as ~ -0.06 in the allowed region. As can be seen in Fig. 11(c), $\mathrm{Re}(C_7'(\mu_b))$ is very sensitive to $\tan\beta$ and also sensitive to T_{D23} for large $\tan\beta \gtrsim 70$, as expected, and is sizable $(-0.05 \lesssim \mathrm{Re}(C_7'(\mu_b)) \lesssim -0.04)$ respecting all the constraints in a significant part of this parameter plane. From Fig. 11(d) we find that $\mathrm{Re}(C_7'(\mu_b))$ is very sensitive to M_{D23}^2, and is sizable $(-0.05 \lesssim \mathrm{Re}(C_7'(\mu_b)) \lesssim -0.04)$ respecting all the constraints in a significant part of this parameter plane.

In Figs. 12 and 13 we show contour plots of $\mathrm{Re}(C_7^{\mathrm{MSSM}}(\mu_b))$ (i.e., the MSSM contributions to $\mathrm{Re}(C_7(\mu_b))$) around the benchmark point P1 in various parameter planes.

Figure 12(a) shows contours of $\mathrm{Re}(C_7^{\mathrm{MSSM}}(\mu_b))$ in the T_{U23}-T_{U32} plane. We see that $\mathrm{Re}(C_7^{\mathrm{MSSM}}(\mu_b))$ is sensitive to T_{U23} and T_{U32}: $|\mathrm{Re}(C_7^{\mathrm{MSSM}}(\mu_b))|$ quickly increases with the increase of T_{U23} and T_{U32} as is expected. We find also that $\mathrm{Re}(C_7^{\mathrm{MSSM}}(\mu_b))$ can be as large as about -0.05 in the allowed region and is sizable $(-0.05 \lesssim \mathrm{Re}(C_7^{\mathrm{MSSM}}(\mu_b)) \lesssim -0.04)$ respecting all the constraints in a significant part of this parameter plane. From Fig. 12(b) we see that $\mathrm{Re}(C_7^{\mathrm{MSSM}}(\mu_b))$ is very sensitive also to T_{U33}

TABLE II. The MSSM parameters for the reference point P1 (in units of GeV or GeV^2 expect for $\tan\beta$). All parameters are defined at scale Q = 1 TeV, except m_A(pole). The parameters that are not shown here are taken to be zero.

$\tan\beta$	M_1	M_2	M_3	μ	m_A(pole)
70	910	1970	2795	800	4970
M_{Q22}^2	M_{Q33}^2	M_{Q23}^2	M_{U22}^2	M_{U33}^2	M_{U23}^2
3630^2	3365^2	-740^2	2755^2	1510^2	-1705^2
M_{D22}^2	M_{D33}^2	M_{D23}^2	T_{U23}	T_{U32}	T_{U33}
2985^2	1270^2	-1820^2	2700	−260	4995
T_{D23}	T_{D32}	T_{D33}	T_{E33}		
−2330	−335	3675	−335		

M_{Q11}^2	M_{U11}^2	M_{D11}^2	M_{L11}^2	M_{L22}^2	M_{L33}^2	M_{E11}^2	M_{E22}^2	M_{E33}^2
4500^2	4500^2	4500^2	1500^2	1500^2	1500^2	1500^2	1500^2	1500^2

TABLE III. Physical masses in GeV of the particles for the scenario of Table II.

$m_{\tilde{\chi}_1^0}$	$m_{\tilde{\chi}_2^0}$	$m_{\tilde{\chi}_3^0}$	$m_{\tilde{\chi}_4^0}$	$m_{\tilde{\chi}_1^+}$	$m_{\tilde{\chi}_2^+}$
800	812	925	2030	809	2030

m_{h^0}	m_{H^0}	m_{A^0}	m_{H^+}
124.9	4970	4970	4997

$m_{\tilde{g}}$	$m_{\tilde{u}_1}$	$m_{\tilde{u}_2}$	$m_{\tilde{u}_3}$	$m_{\tilde{u}_4}$	$m_{\tilde{u}_5}$	$m_{\tilde{u}_6}$
2934	1231	2986	3431	3656	4491	4493

$m_{\tilde{d}_1}$	$m_{\tilde{d}_2}$	$m_{\tilde{d}_3}$	$m_{\tilde{d}_4}$	$m_{\tilde{d}_5}$	$m_{\tilde{d}_6}$
836	3272	3416	3654	4489	4492

$m_{\tilde{\nu}_1}$	$m_{\tilde{\nu}_2}$	$m_{\tilde{\nu}_3}$	$m_{\tilde{l}_1}$	$m_{\tilde{l}_2}$	$m_{\tilde{l}_3}$	$m_{\tilde{l}_4}$	$m_{\tilde{l}_5}$	$m_{\tilde{l}_6}$
1506	1507	1582	1495	1496	1509	1509	1564	1652

TABLE IV. Flavor decompositions of the mass eigenstates $\tilde{u}_{1,2,3}$ and $\tilde{d}_{1,2,3}$ for the scenario of Table II. Shown are the expansion coefficients of the mass eigenstates in terms of the flavor eigenstates. Imaginary parts of the coefficients are negligibly small.

	$\tilde{u}_L$	$\tilde{c}_L$	$\tilde{t}_L$	$\tilde{u}_R$	$\tilde{c}_R$	$\tilde{t}_R$
$\tilde{u}_1$	0	0.0016	0.0992	0	−0.4090	−0.9071
$\tilde{u}_2$	−0.0012	−0.0070	−0.0225	0	0.9104	−0.4130
$\tilde{u}_3$	0.0660	0.2921	0.9491	0	0.0607	0.0770
	$\tilde{d}_L$	$\tilde{s}_L$	$\tilde{b}_L$	$\tilde{d}_R$	$\tilde{s}_R$	$\tilde{b}_R$
$\tilde{d}_1$	0	0	0.0059	0	0.4057	0.9140
$\tilde{d}_2$	0	0.0059	0.0289	0	−0.9137	0.4054
$\tilde{d}_3$	0	0.2898	0.9566	0	0.0245	−0.0172

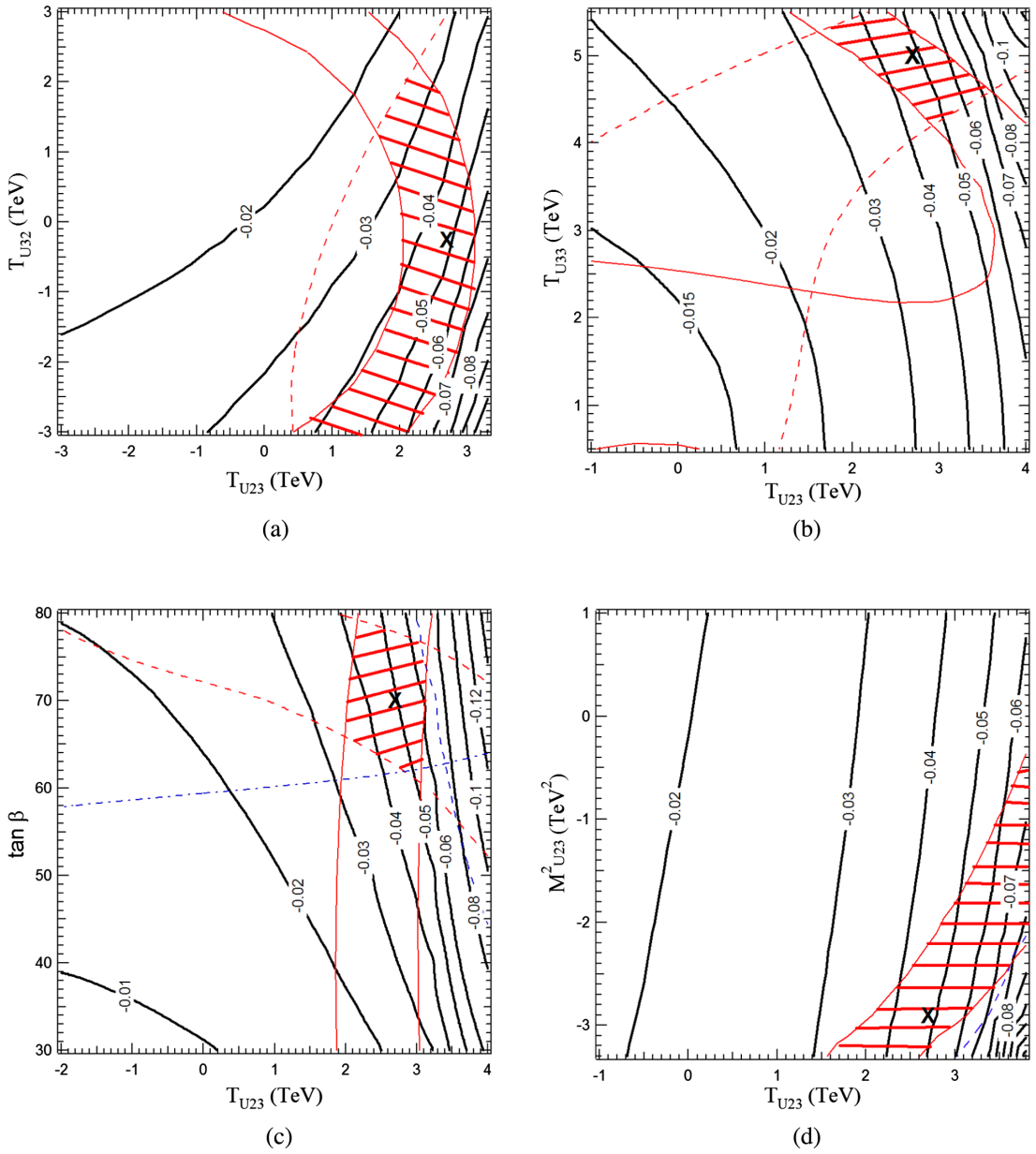

FIG. 10. Contour plots of $\mathrm{Re}(C_7'(\mu_b))$ around the benchmark point P1 in the parameter planes of (a) T_{U23}-T_{U32}, (b) T_{U23}-T_{U33}, (c) T_{U23}- $\tan\beta$, and (d) T_{U23}-M^2_{U23}. The parameters other than the shown ones in each plane are fixed as in Table II. The "X" marks P1 in the plots. The red hatched region satisfies all the constraints in Appendix A. The red solid lines, the nearly vertical blue dashed lines in (c),(d), the red dashed lines in (a),(b),(c) and the blue dash-dotted lines show the m_{h^0} bound, the $\mathrm{B}(b \to s\gamma)$ bound, the $\mathrm{B}(B_s \to \mu^+\mu^-)$ bound, and the $m_{\tilde{d}_1}$ bound, respectively.

(see Fig. 8(c) also), quickly increases with increase of T_{U33} as is expected partly from the important contribution of Fig. 2(b) [see Eq. (10)], and can be as large as about -0.05 in the allowed region. It is sizable $(-0.05 \lesssim \mathrm{Re}(C_7^{\mathrm{MSSM}}(\mu_b)) \lesssim -0.04)$ respecting all the constraints in a significant part of this parameter plane. From Fig. 12(c) we find that $\mathrm{Re}(C_7^{\mathrm{MSSM}}(\mu_b))$ is very sensitive to $\tan\beta$ and T_{U23} as expected, quickly increases with increase of $\tan\beta$ and $T_{U23}(>0)$, and can be as large as ~ -0.05 in the allowed region. As can be seen in Fig. 12(d), $\mathrm{Re}(C_7^{\mathrm{MSSM}}(\mu_b))$ is sensitive to M^2_{U23} and T_{U23} increasing with the increase of $M^2_{U23}(<0)$ and $T_{U23}(>0)$ as expected, and is large $(-0.05 \lesssim \mathrm{Re}(C_7^{\mathrm{MSSM}}(\mu_b)) \lesssim -0.04)$ respecting all the constraints in a significant part of this parameter plane.

Fig. 13(a) shows contours of $\mathrm{Re}(C_7^{\mathrm{MSSM}}(\mu_b))$ in the T_{D23}-T_{D32} plane. We see that $\mathrm{Re}(C_7^{\mathrm{MSSM}}(\mu_b))$ is mildly dependent on T_{D23} and fairly sensitive to T_{D32} around P1 as

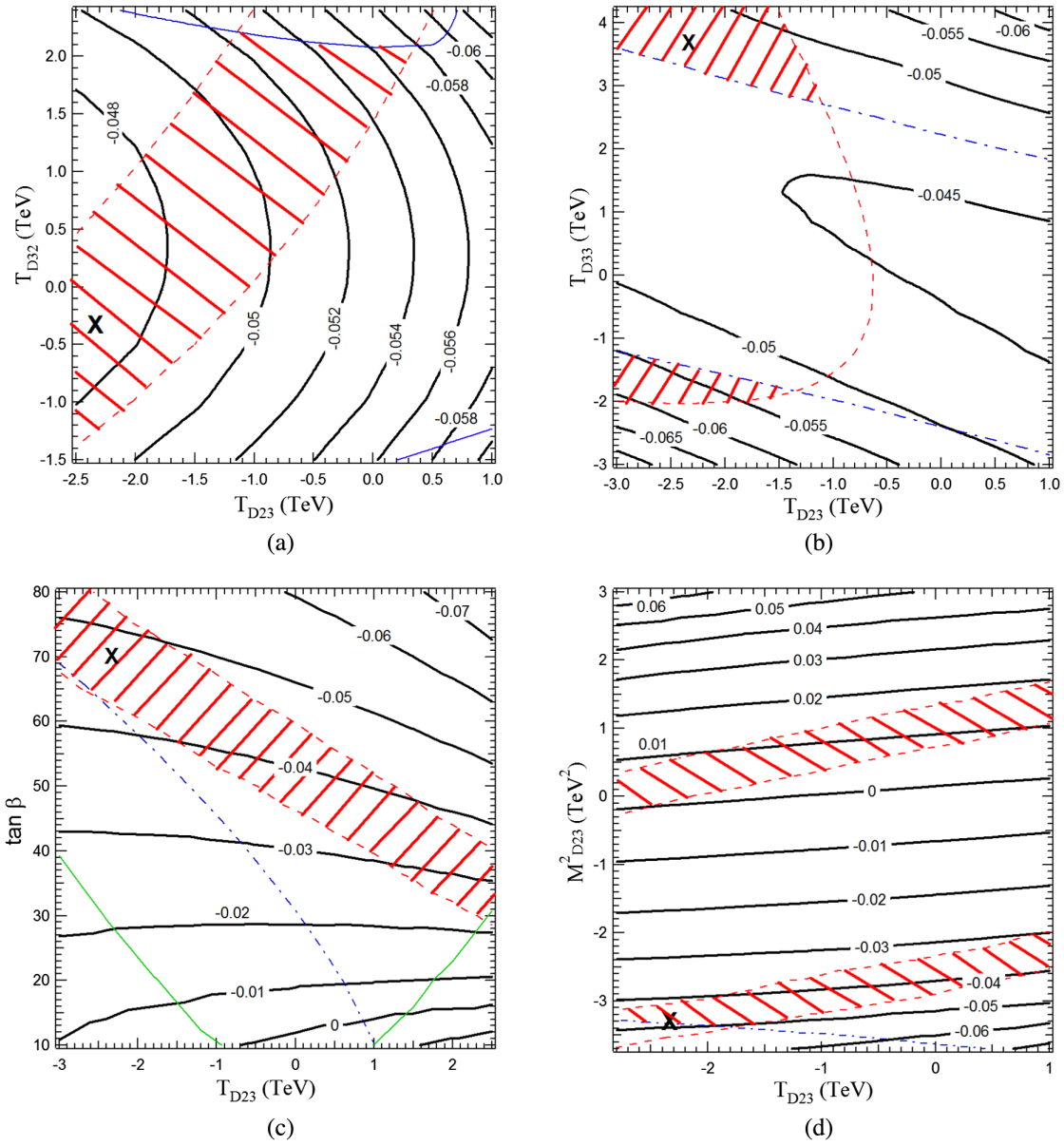

FIG. 11. Contour plots of $\mathrm{Re}(C_7'(\mu_b))$ around the benchmark point P1 in the parameter planes of (a) T_{D23}-T_{D32}, (b) T_{D23}-T_{D33}, (c) T_{D23}- $\tan\beta$, and (d) T_{D23}-M^2_{D23}. The parameters other than the shown ones in each plane are fixed as in Table II. The "X" marks P1 in the plots. The red hatched region satisfies all the constraints in Appendix A. The definitions of the bound lines are the same as in Fig. 10. In addition to these the blue solid lines in (a) and the green solid lines in (c) show the ΔM_{B_s} bound and the vacuum stability bound on T_{D23}, respectively.

is expected partly from the contribution of Fig. 3(b) [see Eq. (10)]. It can be as large as about -0.046 in the allowed region, and is sizable ($-0.046 \lesssim \mathrm{Re}(C_7^{\mathrm{MSSM}}(\mu_b)) \lesssim -0.044$) respecting all the constraints in a significant part of this parameter plane. From Fig. 13(b) we see that $\mathrm{Re}(C_7^{\mathrm{MSSM}}(\mu_b))$ is also fairly sensitive to T_{D33} around P1, can be as large as about -0.045 in the allowed region, and is sizable ($-0.045 \lesssim \mathrm{Re}(C_7^{\mathrm{MSSM}}(\mu_b)) \lesssim -0.044$) respecting all the constraints in a significant part of this parameter plane. From Fig. 13(c) we find that $\mathrm{Re}(C_7^{\mathrm{MSSM}}(\mu_b))$ is very sensitive to $\tan\beta$ quickly increasing with the increase of $\tan\beta$ as expected, can be as large as ~ -0.05 in the allowed region, and is sizable ($-0.05 \lesssim \mathrm{Re}(C_7^{\mathrm{MSSM}}(\mu_b)) \lesssim -0.04$) respecting all the constraints in a significant part of this parameter plane. As can be seen in Fig. 13(d), $\mathrm{Re}(C_7^{\mathrm{MSSM}}(\mu_b))$ is mildly dependent on M^2_{D23} around this benchmark point P1, can be as large as about -0.044 in the allowed region, and is sizable ($-0.044 \lesssim \mathrm{Re}(C_7^{\mathrm{MSSM}}(\mu_b)) \lesssim -0.043$) respecting all the constraints in a significant part of this parameter plane.

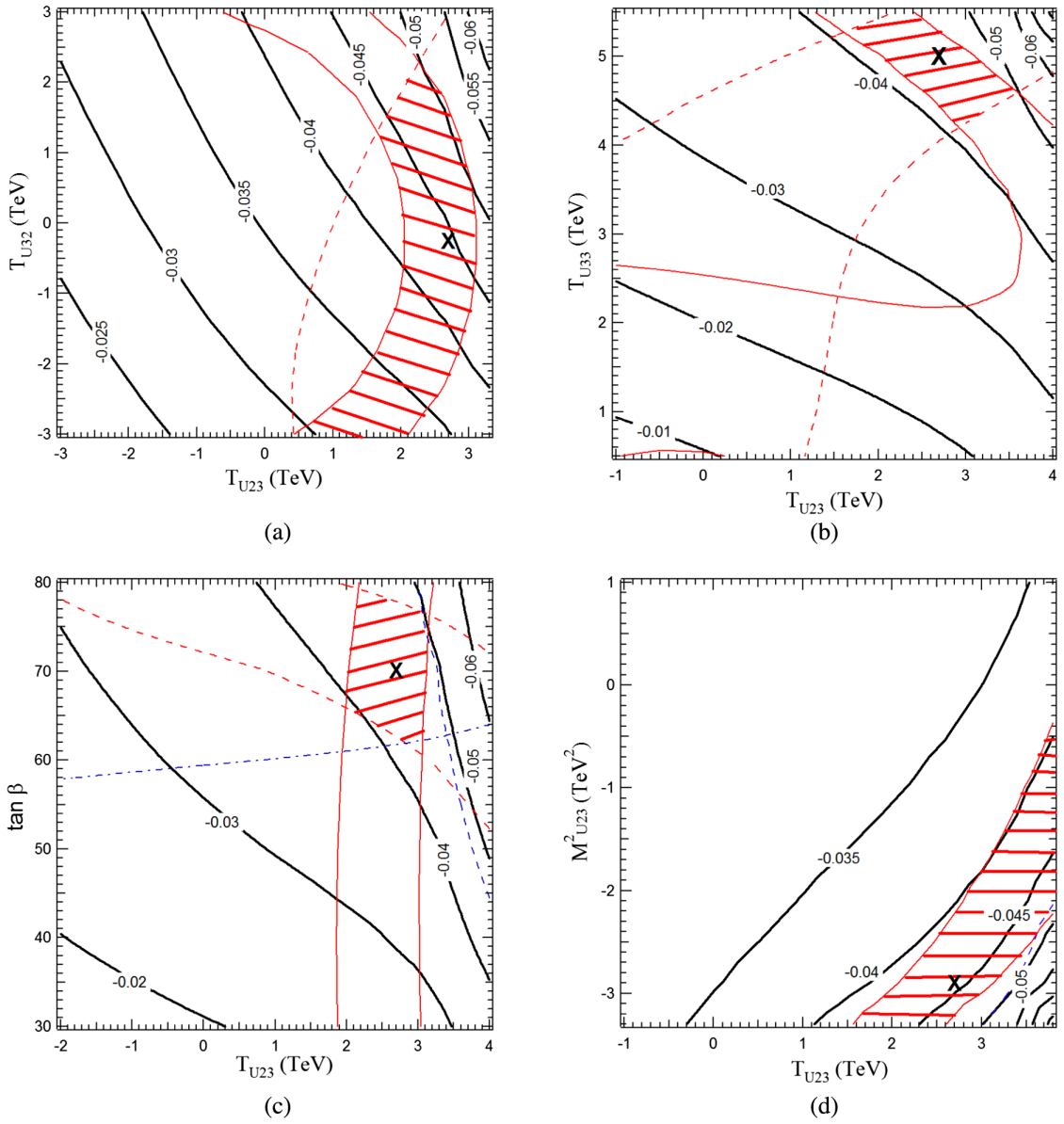

FIG. 12. Contour plots of $\mathrm{Re}(C_7^{\mathrm{MSSM}}(\mu_b))$ around the benchmark point P1 in the parameter planes of (a) T_{U23}-T_{U32}, (b) T_{U23}-T_{U33}, (c) T_{U23}- $\tan\beta$, and (d) T_{U23}-M^2_{U23}. The parameters other than the shown ones in each plane are fixed as in Table II. The "X" marks P1 in the plots. The red hatched region satisfies all the constraints in Appendix A. The definitions of the bound lines are the same as those in Fig. 10.

As the gluino is very heavy (∼3 TeV) around the reference point P1 (see Table III), the down-type squark-gluino loop contributions to $\mathrm{Re}(C_7'(\mu_b))$ and $\mathrm{Re}(C_7^{\mathrm{MSSM}}(\mu_b))$ are suppressed there, which partly explains the rather mild dependences of $\mathrm{Re}(C_7'(\mu_b))$ and $\mathrm{Re}(C_7^{\mathrm{MSSM}}(\mu_b))$ on the down-type squark parameters T_{D23}, T_{D32}, T_{D33} around P1 as is seen in Figs. 11 and 13, respectively.

Before closing this section we comment on the renormalization scale dependence of the WCs $C_7^{\mathrm{MSSM}}(\mu_b)$ and $C_7'(\mu_b)$. For the reference scenario P1 we have the following result at LO: $(\mathrm{Re}(C_7(\mu_b/2)), \mathrm{Im}(C_7(\mu_b/2)) = (-0.405, -4.04\times10^{-4})$, $(\mathrm{Re}(C_7^{\mathrm{MSSM}}(\mu_b/2)), \mathrm{Im}(C_7^{\mathrm{MSSM}}(\mu_b/2)) = (-0.0379, -4.04 \times 10^{-4})$ and $(\mathrm{Re}(C_7'(\mu_b/2)), \mathrm{Im}(C_7'(\mu_b/2)) = (-0.0350, -1.34 \times 10^{-3})$; $(\mathrm{Re}(C_7(2\mu_b)), \mathrm{Im}(C_7(2\mu_b)) = (-0.341, -6.19\times10^{-4})$, $(\mathrm{Re}(C_7^{\mathrm{MSSM}}(2\mu_b)), \mathrm{Im}(C_7^{\mathrm{MSSM}}(2\mu_b)) = (-0.0499, -6.20 \times 10^{-4})$ and $(\mathrm{Re}(C_7'(2\mu_b)), \mathrm{Im}(C_7'(2\mu_b)) = (-0.0594, -2.28 \times 10^{-3})$, where $\mu_b = 4.8$ GeV. We see that the scale dependence of the WCs at the b-quark mass scale is significant at LO in agreement with Refs. [5–7] and hence that it is important to compute the WCs at higher order (NLO/NNLO) level in

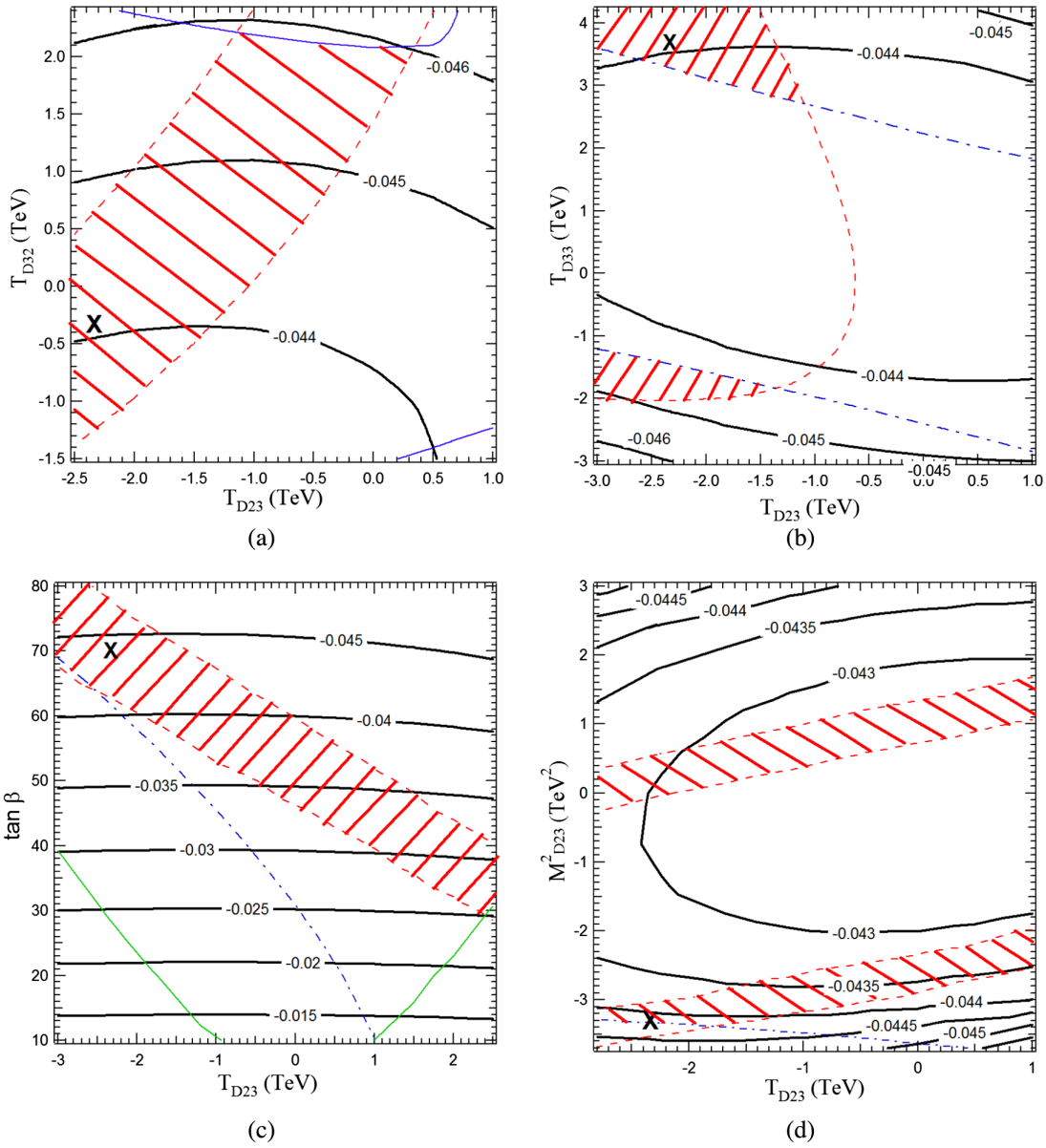

FIG. 13. Contour plots of $\mathrm{Re}(C_7^{\mathrm{MSSM}}(\mu_b))$ around the benchmark point P1 in the parameter planes of (a) T_{D23}-T_{D32}, (b) T_{D23}-T_{D33}, (c) T_{D23}- $\tan\beta$, and (d) T_{D23}-M^2_{D23}. The parameters other than the shown ones in each plane are fixed as in Table II. The "X" marks P1 in the plots. The red hatched region satisfies all the constraints in Appendix A. The definitions of the bound lines are the same as those in Fig. 11.

order to reduce this scale-dependence uncertainties. In [21] MSSM loop contributions to the WCs $C_{7,8}(\mu_W)$ and $C'_{7,8}(\mu_W)$ are calculated at NLO in the MSSM with QFV. So far, however, there is no complete NLO computation of the WCs $C_7(\mu_b)$ and $C'_7(\mu_b)$ in the MSSM with QFV.[6]

[6]In principle the MSSM loop contributions to $C_7(\mu_b)$ and $C'_7(\mu_b)$ at NLO can be obtained from $C_i(\mu_W)$ and $C'_i(\mu_W)$ (i = 1-8) calculated at NLO in the MSSM by using QCD RG scale evolution from the scale μ_W down to μ_b at NLL (next-to-leading log) level [7], where $C_i(\mu_W)$ and $C'_i(\mu_W)$ (i = 1-6) are the Wilson coefficients of the four-quark operators.

V. CONCLUSIONS

We have studied SUSY effects on $C_7(\mu_b)$ and $C'_7(\mu_b)$ which are the Wilson coefficients for $b \to s\gamma$ at b-quark mass scale μ_b and are closely related to radiative B-meson decays. The SUSY-loop contributions to the $C_7(\mu_b)$ and $C'_7(\mu_b)$ are calculated at LO in the Minimal Supersymmetric Standard Model with general quark-flavor violation. For the first time we have performed a systematic MSSM parameter scan for the WCs $C_7(\mu_b)$ and $C'_7(\mu_b)$ respecting all the relevant constraints, i.e., the theoretical constraints from vacuum stability conditions and the experimental constraints, such as those from K- and B-meson data and

electroweak precision data, as well as recent limits on SUSY particle masses and the 125 GeV Higgs boson data from LHC experiments. From the parameter scan, we have found the following:

(i) The MSSM contribution to $\mathrm{Re}(C_7(\mu_b))$ can be as large as $\sim \pm 0.05$ which could correspond to about 3σ significance of NP (New Physics) signal in future Belle II and LHCb Upgrade experiments.
(ii) The MSSM contribution to $\mathrm{Re}(C_7'(\mu_b))$ can be as large as ~ -0.08 which could correspond to about 4σ significance of NP signal in future Belle II and LHCb Upgrade experiments.
(iii) These large MSSM contributions to the WCs are mainly due to (i) large scharm-stop mixing and large scharm/stop involved trilinear couplings T_{U23}, T_{U32} and T_{U33}, (ii) large sstrange-sbottom mixing and large sstrange-sbottom involved trilinear couplings T_{D23}, T_{D32} and T_{D33}, and (iii) large bottom Yukawa coupling Y_b for large $\tan\beta$ and large top Yukawa coupling Y_t.

Moreover, we have pointed out the following:

(i) It is very important to reduce the (theoretical and experimental) errors of the WCs $C_7'(\mu_b)$ and $C_7^{\mathrm{NP}}(\mu_b)$ obtained (extracted) from the future experiments at Belle II and the LHCb Upgrade. An improvement in precision of both theory and experiment by a factor about 1.5 or so would be very important in view of NP search (such as SUSY search). Therefore, we strongly encourage theorists and experimentalists to challenge this task.
(ii) On the other hand, it is also very important to reduce the theoretical errors of the MSSM contributions to the WCs $C_7'(\mu_b)$ and $C_7(\mu_b)$ by performing higher order computations such as those at NLO/NNLO level.

In case such large New Physics contributions to the WCs, i.e., such large deviations of the WCs from their SM values, are really observed in the future experiments at Belle II and the LHCb Upgrade, this could be the imprint of QFV SUSY (the MSSM with general QFV) and would encourage to perform further studies of the WCs $C_7'(\mu_b)$ and $C_7^{\mathrm{MSSM}}(\mu_b)$ at NLO/NNLO level in this model.

ACKNOWLEDGMENTS

We would like to thank W. Porod for helpful discussions, especially for the permanent support concerning SPheno. VRV is funded by Bundesministerium für Verkehr, Innovation und Technologie (BMVIT), Bundesministerium für Digitalisierung und Wirtschaftsstandort (BMDW), Amt der Steiermärkischen Landesregierung, Steirische Wirtschaftsförderungsgesellschaft (SFG) and Vienna Business Agency in the scope of COMET—Competence Centers for Excellent Technologies (854174) which is managed by Österreichische Forschungsförderungsgesellschaft (FFG).

APPENDIX A: THEORETICAL AND EXPERIMENTAL CONSTRAINTS

The experimental and theoretical constraints taken into account in the present work are discussed in detail in [43]. Here we list the updated constraints from K- and B-physics and those on the Higgs boson mass and couplings in Table V. For the mass of the Higgs boson h^0, taking the combination of the ATLAS and CMS measurements $m_{h^0} = 125.09 \pm 0.24$ GeV [52] and adding the theoretical uncertainty of $\sim \pm 3$ GeV [53] linearly to the experimental uncertainty at 2σ, we take $m_{h^0} = 125.09 \pm 3.48$ GeV. The h^0 couplings that receive SUSY QFV effects significantly are $C(hbb)$ [41], $C(hcc)$ [56], $C(hgg)$ and $C(h\gamma\gamma)$ [42].[7] The measurement of $C(hcc)$ is very difficult due to huge QCD backgrounds at LHC; there is no significant experimental data on $C(hcc)$ at this moment. Hence, the relevant h^0 couplings to be compared with the LHC observations are $C(hbb)$, $C(hgg)$ and $C(h\gamma\gamma)$. Therefore, we list the LHC data on $C(hbb)$ (κ_b), $C(hgg)$ (κ_g) and $C(h\gamma\gamma)$ (κ_γ) in Table V.

As the constraints from the decays $B \to D^{(*)}\tau\nu$ are unclear due to large theoretical uncertainties [56],[8] we do not take these constraints into account in our paper. As the issues of possible anomalies of $R(D^{(*)}) = B(B \to D^{(*)}\tau\nu)/B(B \to D^{(*)}\ell\nu)$ with $\ell = e$ or μ and $R_{K^{(*)}} = B(B \to K^{(*)}e^+e^-)/B(B \to K^{(*)}\mu^+\mu^-)$ are not yet settled [45,49], we do not take the constraints from these ratios into account either. In [25] the QFV decays $t \to qh^0$ with $q = u$, c, have been studied in the general MSSM with QFV. It is found that these decays cannot be visible at the current and high luminosity LHC runs due to the very small decay branching ratios $\mathrm{B}(t \to qh^0)$, giving no significant constraint on the $\tilde{c} - \tilde{t}$ mixing.

We comment on the very recent data on the anomalous magnetic moment of muon a_μ from the Fermilab experiment [59]. The Fermilab data has been combined with the previous BNL data [60] resulting in 4.2σ discrepancy between the experimental data and the SM prediction.[9] In our scenario with heavy sleptons/sneutrinos with masses of about 1.5 TeV the MSSM loop contributions to a_μ are so

[7] Precisely speaking, in principle, $C(htt)$ coupling could also receive SUSY QFV effects significantly. However, predicting the (effective) coupling $C(htt)$ at loop levels in the MSSM is very difficult since its theoretical definition in the context of $t\bar{t}h$ production at LHC is unclear [57].

[8] As pointed out in [58], the theoretical predictions (in the SM and MSSM) on $\mathrm{B}(B \to Dl\nu)$ and $\mathrm{B}(B \to D^*l\nu)$ ($l = \tau, \mu, e$) have potentially large theoretical uncertainties due to the theoretical assumptions on the form factors at the BDW^+ and BD^*W^+ vertices (also at the BDH^+ and BD^*H^+ vertices in the MSSM). Hence the constraints from these decays are unclear.

[9] It is worth noting that according to the recent computation of the leading order hadronic vacuum polarization contribution to a_μ using lattice QCD [61], the discrepancy between the experimental data and the SM prediction is only about 1.6σ.

TABLE V. Constraints on the MSSM parameters from the K- and B-meson data relevant mainly for the mixing between the second and the third generations of squarks and from the data on the h^0 mass and couplings κ_b, κ_g, κ_γ. The fourth column shows constraints at 95% CL obtained by combining the experimental error quadratically with the theoretical uncertainty, except for $B(K_L^0 \to \pi^0\nu\bar{\nu})$, m_{h^0} and $\kappa_{b,g,\gamma}$.

Observable	Exp. data	Theor. uncertainty	Constr. (95% CL)
$10^3 \times \lvert\epsilon_K\rvert$	2.228 ± 0.011 (68% CL) [24]	± 0.28 (68% CL) [44]	2.228 ± 0.549
$10^{15} \times \Delta M_K$ [GeV]	3.484 ± 0.006 (68% CL) [24]	± 1.2 (68% CL) [44]	3.484 ± 2.352
$10^9 \times \mathrm{B}(K_L^0 \to \pi^0\nu\bar{\nu})$	< 3.0 (90% CL) [24]	± 0.002 (68% CL) [24]	< 3.0 (90% CL)
$10^{10} \times \mathrm{B}(K^+ \to \pi^+\nu\bar{\nu})$	1.7 ± 1.1 (68% CL) [24]	± 0.04 (68% CL) [24]	$1.7^{+2.16}_{-1.70}$
ΔM_{B_s} [ps^{-1}]	17.757 ± 0.021 (68% CL) [24,45]	± 2.7 (68% CL) [46]	17.757 ± 5.29
$10^4 \times \mathrm{B}(b \to s\gamma)$	3.32 ± 0.15 (68% CL) [24,45]	± 0.23 (68% CL) [11]	3.32 ± 0.54
$10^6 \times \mathrm{B}(b \to s l^+ l^-)$	$1.60^{+0.48}_{-0.45}$ (68% CL) [47]	± 0.11 (68% CL) [48]	$1.60^{+0.97}_{-0.91}$
($l = e$ or μ)			
$10^9 \times \mathrm{B}(B_s \to \mu^+\mu^-)$	$2.69^{+0.37}_{-0.35}$ (68% CL) [49]	± 0.23 (68% CL) [50]	$2.69^{+0.85}_{-0.82}$
$10^4 \times \mathrm{B}(B^+ \to \tau^+\nu)$	1.06 ± 0.19 (68% CL) [45]	± 0.29 (68% CL) [51]	1.06 ± 0.69
m_{h^0} [GeV]	125.09 ± 0.24 (68% CL) [52]	± 3 [53]	125.09 ± 3.48
κ_b	$1.06^{+0.37}_{-0.35}$ (95% CL) [54]		$1.06^{+0.37}_{-0.35}$ (ATLAS)
	$1.17^{+0.53}_{-0.61}$ (95% CL) [55]		$1.17^{+0.53}_{-0.61}$ (CMS)
κ_g	$1.03^{+0.14}_{-0.12}$ (95% CL) [54]		$1.03^{+0.14}_{-0.12}$ (ATLAS)
	$1.18^{+0.31}_{-0.27}$ (95% CL) [55]		$1.18^{+0.31}_{-0.27}$ (CMS)
κ_γ	1.00 ± 0.12 (95% CL) [54]		1.00 ± 0.12 (ATLAS)
	$1.07^{+0.27}_{-0.29}$ (95% CL) [55]		$1.07^{+0.27}_{-0.29}$ (CMS)

small that they cannot explain the discrepancy between the new data and the SM prediction. Therefore, in the context of our scenario, this discrepancy should be explained by the loop contributions of another new physics coexisting with SUSY.

In addition to these we also require our scenarios to be consistent with the following experimental constraints:

(i) The LHC limits on sparticle masses (at 95% CL) [62–66]:

We impose conservative limits for safety though actual limits are somewhat weaker than those shown here. In the context of simplified models, gluino masses $m_{\tilde{g}} \lesssim 2.35$ TeV are excluded for $m_{\tilde{\chi}_1^0} < 1.55$ TeV. There is no gluino mass limit for $m_{\tilde{\chi}_1^0} > 1.55$ TeV. The 8-fold degenerate first two generation squark masses are excluded below 1.92 TeV for $m_{\tilde{\chi}_1^0} < 0.9$ TeV. There is no limit on the masses for $m_{\tilde{\chi}_1^0} > 0.9$ TeV. We impose this squark mass limit on $m_{\tilde{u}_3}$ and $m_{\tilde{d}_3}$. Bottom-squark masses are excluded below 1.26 TeV for $m_{\tilde{\chi}_1^0} < 0.73$ TeV. There is no bottom-squark mass limit for $m_{\tilde{\chi}_1^0} > 0.73$ TeV. Here the bottom-squark mass means the lighter sbottom mass $m_{\tilde{b}_1}$. We impose this limit on $m_{\tilde{d}_1}$ since $\tilde{d}_1 \sim \tilde{b}_R$ (see Table IV). A typical top-squark mass lower limit is ~1.26 TeV for $m_{\tilde{\chi}_1^0} < 0.62$ TeV. There is no top-squark mass limit for $m_{\tilde{\chi}_1^0} > 0.62$ TeV. Here the top-squark mass means the lighter stop mass $m_{\tilde{t}_1}$. We impose this limit on $m_{\tilde{u}_1}$ since $\tilde{u}_1 \sim \tilde{t}_R$ (see Table IV). For sleptons/sneutrinos heavier than the lighter chargino $\tilde{\chi}_1^\pm$ and the second neutralino $\tilde{\chi}_2^0$, the mass limits are $m_{\tilde{\chi}_1^\pm}, m_{\tilde{\chi}_2^0} > 0.74$ TeV for $m_{\tilde{\chi}_1^0} \lesssim 0.3$ TeV and there is no $m_{\tilde{\chi}_1^\pm}$, $m_{\tilde{\chi}_2^0}$ limits for $m_{\tilde{\chi}_1^0} > 0.3$ TeV; For sleptons/sneutrinos lighter than $\tilde{\chi}_1^\pm$ and $\tilde{\chi}_2^0$, the mass limits are $m_{\tilde{\chi}_1^\pm}, m_{\tilde{\chi}_2^0} > 1.15$ TeV for $m_{\tilde{\chi}_1^0} \lesssim 0.72$ TeV and there is no $m_{\tilde{\chi}_1^\pm}$, $m_{\tilde{\chi}_2^0}$ limits for $m_{\tilde{\chi}_1^0} > 0.72$ TeV. For mass degenerate selectrons $\tilde{e}_{L,R}$ and smuons $\tilde{\mu}_{L,R}$, masses below 0.7 TeV are excluded for $m_{\tilde{\chi}_1^0} < 0.41$ TeV. For mass degenerate staus $\tilde{\tau}_L$ and $\tilde{\tau}_R$, masses below 0.39 TeV are excluded for $m_{\tilde{\chi}_1^0} < 0.14$ TeV. There is no sneutrino $\tilde{\nu}$ mass limit from LHC yet. Sneutrino masses below 94 GeV are excluded by LEP200 experiment [24].

(ii) The constraint on $(m_{A^0,H^+}, \tan\beta)$ (at 95% CL) from searches for the MSSM Higgs bosons H^0, A^0 and H^+ at LHC, [67–73], where H^0 is the heavier CP-even Higgs boson.

(iii) The experimental limit on SUSY contributions on the electroweak ρ parameter [74]: $\Delta\rho(\mathrm{SUSY}) < 0.0012$.

Furthermore, we impose the following theoretical constraints from the vacuum stability conditions for the trilinear coupling matrices [75]:

$$|T_{U\alpha\alpha}|^2 < 3Y_{U\alpha}^2(M_{Q\alpha\alpha}^2 + M_{U\alpha\alpha}^2 + m_2^2), \quad \text{(A1)}$$

$$|T_{D\alpha\alpha}|^2 < 3Y_{D\alpha}^2(M_{Q\alpha\alpha}^2 + M_{D\alpha\alpha}^2 + m_1^2), \quad \text{(A2)}$$

$$|T_{U\alpha\beta}|^2 < Y_{U\gamma}^2(M_{Q\beta\beta}^2 + M_{U\alpha\alpha}^2 + m_2^2), \quad \text{(A3)}$$

$$|T_{D\alpha\beta}|^2 < Y_{D\gamma}^2(M_{Q\beta\beta}^2 + M_{D\alpha\alpha}^2 + m_1^2), \quad \text{(A4)}$$

where $\alpha, \beta = 1, 2, 3$, $\alpha \neq \beta$; $\gamma = \mathrm{Max}(\alpha, \beta)$ and $m_1^2 = (m_{H^+}^2 + m_Z^2 \sin^2\theta_W)\sin^2\beta - \frac{1}{2}m_Z^2$, $m_2^2 = (m_{H^+}^2 + m_Z^2 \sin^2\theta_W) \times \cos^2\beta - \frac{1}{2}m_Z^2$. The Yukawa couplings of the up-type and down-type quarks are $Y_{U\alpha} = \sqrt{2}m_{u_\alpha}/v_2 = \frac{g}{\sqrt{2}}\frac{m_{u_\alpha}}{m_W \sin\beta}$ $(u_\alpha = u, c, t)$ and $Y_{D\alpha} = \sqrt{2}m_{d_\alpha}/v_1 = \frac{g}{\sqrt{2}}\frac{m_{d_\alpha}}{m_W \cos\beta}$ $(d_\alpha = d, s, b)$, with m_{u_α} and m_{d_α} being the running quark masses at the scale $Q = 1$ TeV and g being the SU(2) gauge coupling. All soft SUSY-breaking parameters are given at $Q = 1$ TeV. As SM parameters we take $m_Z = 91.2$ GeV and the on-shell top-quark mass $m_t = 172.9$ GeV [24].

[1] E. Kou *et al.* (Belle II Collaboration), Prog. Theor. Exp. Phys. **2019**, 123C01 (2019); **2020**, 029201(E) (2020).
[2] R. Aaij *et al.* (LHCb Collaboration), arXiv:1808.08865.
[3] J. Albrecht, F. Bernlochner, M. Kenzie, S. Reichert, D. Straub, and A. Tully, arXiv:1709.10308.
[4] A. Paul and D. M. Straub, J. High Energy Phys. 04 (2017) 027.
[5] A. Ali and C. Greub, Phys. Lett. B **293**, 226 (1992).
[6] A. Ali, C. Greub, and T. Mannel, Rare B decays in the standard model, in *Proceedings of ECFA Workshop on B-Meson Factory*, edited by R. Aleksan and A. Ali (DESY, Hamburg, 1993).
[7] A. J. Buras, M. Misiak, M. Muenz, and S. Pokorski, Nucl. Phys. **B424**, 374 (1994).
[8] K. Chetyrkin, M. Misiak, and M. Munz, Phys. Lett. B **400**, 206 (1997); **425**, 414(E) (1998).
[9] A. L. Kagan and M. Neubert, Eur. Phys. J. C **7**, 5 (1999).
[10] A. J. Buras, arXiv:1102.5650, and references therein.
[11] M. Misiak *et al.*, Phys. Rev. Lett. **114**, 221801 (2015).
[12] M. Misiak, A. Rehman, and M. Steinhauser, J. High Energy Phys. 06 (2020) 175.
[13] F. Borzumati and C. Greub, Phys. Rev. D **58**, 074004 (1998).
[14] M. Ciuchini, G. Degrassi, P. Gambino, and G. F. Giudice, Nucl. Phys. **B527**, 21 (1998).
[15] K. Kiers, A. Soni, and G.-H. Wu, Phys. Rev. D **62**, 116004 (2000).
[16] T. Goto, Y. Okada, and Y. Shimizu, Phys. Rev. D **58**, 094006 (1998).
[17] T. Besmer, C. Greub, and T. Hurth, Nucl. Phys. **B609**, 359 (2001).
[18] L. Everett, G. L. Kane, S. Rigolin, L. T. Wang, and T. T. Wang, J. High Energy Phys. 01 (2002) 022.
[19] T. Hurth, E. Lunghi, and W. Porod, Nucl. Phys. **B704**, 56 (2005).
[20] E. Lunghi and J. Matias, J. High Energy Phys. 04 (2007) 058.
[21] C. Greub, T. Hurth, V. Pilipp, C. Schüpbach, and M. Steinhauser, Nucl. Phys. **B853**, 240 (2011).
[22] B. C. Allanach *et al.*, Comput. Phys. Commun. **180**, 8 (2009).
[23] F. Gabbiani, E. Gabrielli, A. Masiero, and L. Silvestrini, Nucl. Phys. **B477**, 321 (1996).
[24] P. A. Zyla *et al.* (Particle Data Group), Prog. Theor. Exp. Phys. **2020**, 083C01 (2020).
[25] A. Dedes, M. Paraskevas, J. Rosiek, K. Suxho, and K. Tamvakis, J. High Energy Phys. 11 (2014) 137.
[26] W. Porod, Comput. Phys. Commun. **153**, 275 (2003).
[27] W. Porod and F. Staub, Comput. Phys. Commun. **183**, 2458 (2012).
[28] D. M. Pierce, J. A. Bagger, K. T. Matchev, and R.-J. Zhang, Nucl. Phys. **B491**, 3 (1997).
[29] I. S. Choi, S. Y. Choi, and H. S. Song, Phys. Rev. D **41**, 1695 (1990).
[30] Y. Grossman and D. Pirjol, J. High Energy Phys. 06 (2000) 029.
[31] D. Becirevic and E. Schneider, Nucl. Phys. **B854**, 321 (2012).
[32] R. Aaij *et al.* (LHCb Collaboration), J. High Energy Phys. 04 (2015) 064.
[33] D. Atwood, M. Gronau, and A. Soni, Phys. Rev. Lett. **79**, 185 (1997); D. Atwood, T. Gershon, M. Hazumi, and A. Soni, Phys. Rev. D **71**, 076003 (2005).
[34] Y. Ushiroda *et al.* (Belle Collaboration), Phys. Rev. D **74**, 111104 (2006).
[35] B. Aubert *et al.* (*BABAR* Collaboration), Phys. Rev. D **78**, 071102 (2008).
[36] F. Muheim, Y. Xie, and R. Zwicky, Phys. Lett. B **664**, 174 (2008).
[37] R. Aaij *et al.* (LHCb Collaboration), Phys. Rev. Lett. **118**, 021801 (2017).
[38] R. Aaij *et al.* (LHCb Collaboration), J. High Energy Phys. 12 (2020) 081.
[39] F. Borzumati, C. Greub, T. Hurth, and D. Wyler, Phys. Rev. D **62**, 075005 (2000).
[40] T. Browder, SuperKEKB/Belle II upgrades, Proceedings of the Snowmass Community Planning Meeting—Virtual, 5–8 October 2020, https://indico.fnal.gov/event/44870/contributions/199272/.
[41] H. Eberl, E. Ginina, A. Bartl, K. Hidaka, and W. Majerotto, J. High Energy Phys. 06 (2016) 143.
[42] H. Eberl, K. Hidaka, and E. Ginina, Int. J. Mod. Phys. A **34**, 1950120 (2019).

[43] H. Eberl, E. Ginina, and K. Hidaka, Eur. Phys. J. C **77**, 189 (2017).

[44] J. Brod and M. Gorbahn, Phys. Rev. Lett. **108**, 121801 (2012).

[45] Y. Amhis *et al.* (Heavy Flavor Averaging Group (HFLAV)), Eur. Phys. J. C **81**, 226 (2021).

[46] T. Jubb, M. Kirk, A. Lenz, and G. Tetlalmatzi-Xolocotzi, Nucl. Phys. **B915**, 431 (2017); M. Artuso, G. Borissov, and A. Lenz, Rev. Mod. Phys. **88**, 045002 (2016).

[47] J. P. Lees *et al.* (*BABAR* Collaboration), Phys. Rev. Lett. **112**, 211802 (2014).

[48] T. Huber, T. Hurth, and E. Lunghi, Nucl. Phys. **B802**, 40 (2008).

[49] Y. Amhis, *Proceedings of the 40th International Conference on High Energy Physics, virtual conference (ICHEP2020), 2020, Prague, Czech Republic*, PoS ICHEP2020, (Proceedings of Science, Trieste, 2021).

[50] C. Bobeth, M. Gorbahn, T. Hermann, M. Misiak, E. Stamou, and M. Steinhauser, Phys. Rev. Lett. **112**, 101801 (2014).

[51] J. M. Roney, *Proceedings of the 26th International Symposium on Lepton Photon Interactions at High Energies, San Francisco, USA, 2013* (World Scientific, Singapore, 2014).

[52] ATLAS and CMS Collaborations, Phys. Rev. Lett. **114**, 191803 (2015).

[53] S. Borowka, T. Hahn, S. Heinemeyer, G. Heinrich, and W. Hollik, Eur. Phys. J. C **75**, 424 (2015).

[54] ATLAS Collaboration, Phys. Rev. D **101**, 012002 (2020).

[55] CMS Collaboration, Eur. Phys. J. C **79**, 421 (2019).

[56] A. Bartl, H. Eberl, E. Ginina, K. Hidaka, and W. Majerotto, Phys. Rev. D **91**, 015007 (2015).

[57] P. Wu, W.-G. Ma, H.-S. Hou, R.-Y. Zhang, L. Han, and Y. Jiang, Phys. Lett. B **618**, 209 (2005); S. Dittmaier, P. Häfliger, M. Krämer, M. Spira, and M. Walser, Phys. Rev. D **90**, 035010 (2014).

[58] U. Nierste, S. Trine, and S. Westhoff, Phys. Rev. D **78**, 015006 (2008); see also references therein.

[59] Muon g-2 Collaboration, Phys. Rev. Lett. **126**, 141801 (2021).

[60] G. Bennett *et al.* (Muon g–2 Collaboration), Phys. Rev. D **73**, 072003 (2006).

[61] S. Borsanyi *et al.*, Nature (London) **593**, 51 (2021).

[62] F. Moortgat, *Proceedings of the 29th International Symposium on Lepton Photon Interactions at High Energies (LP2019), Toronto, Canada, 2019*, PoS LeptonPhoton2019, (Proceedings of Science, Trieste, 2019).

[63] C. Botta, *Proceedings of the 40th International Conference on High Energy Physics, virtual conference (ICHEP2020), 2020, Prague, Czech Republic*, PoS ICHEP2020, (Proceedings of Science, Trieste, 2021); S. Alderweireldt, *Proceedings of the 40th International Conference on High Energy Physics, virtual conference (ICHEP2020), 2020, Prague, Czech Republic* PoS ICHEP2020, (Proceedings of Science, Trieste, 2021).

[64] ATLAS Collaboration, ATLAS PUB Note, SUSY May 2020 Summary Plot Update, Report No. ATL-PHYS-PUB-2020-013; See also the following Web Page: Summary plots from the ATLAS Supersymmetry physics group, https://atlas.web.cern.ch/Atlas/GROUPS/PHYSICS/CombinedSummaryPlots/SUSY/.

[65] See the following Web Page: Run 2 Summary plots—13 TeV, https://twiki.cern.ch/twiki/bin/view/CMSPublic/PhysicsResultsSUS#Run_2_Summary_plots_13_TeV.

[66] ATLAS Collaboration, J. High Energy Phys. 02 (2021) 143.

[67] ATLAS Collaboration, Phys. Rev. Lett. **125**, 051801 (2020).

[68] CMS Collaboration, J. High Energy Phys. 09 (2018) 007.

[69] ATLAS Collaboration, J. High Energy Phys. 11 (2018) 085.

[70] ATLAS Collaboration, J. High Energy Phys. 06 (2021) 145.

[71] ATLAS Collaboration, J. High Energy Phys. 09 (2018) 139.

[72] CMS Collaboration, J. High Energy Phys. 01 (2020) 096.

[73] CMS Collaboration, J. High Energy Phys. 07 (2019) 142.

[74] G. Altarelli, R. Barbieri, and F. Caravaglios, Int. J. Mod. Phys. A **13**, 1031 (1998).

[75] J. A. Casas and S. Dimopoulos, Phys. Lett. B **387**, 107 (1996).